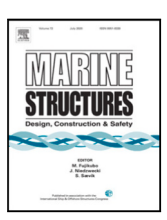
FISEVIER

Contents lists available at ScienceDirect

Marine Structures

journal homepage: www.elsevier.com/locate/marstruc



Underactuated control and analysis of single blade installation using a jackup installation vessel and active tugger line force control

Zhengru Ren ^a, Xingwei Zhen ^{b,*}, Zhiyu Jiang ^c, Zhen Gao ^d, Ye Li ^e, Wei Shi ^f

- ^a Institute for Ocean Engineering, Shenzhen International Graduate School, Tsinghua University, China
- ^b School of Naval Architecture and Ocean Engineering, Dalian University of Technology, Dalian, China
- ^c Department of Engineering Sciences, University of Agder, NO-4879, Grimstad, Norway
- ^d Department of Marine Technology, Norwegian University of Science and Technology, NO-7491, Trondheim, Norway
- ^e Multiple Function Towing Tank Laboratory, State Key Laboratory of Ocean Engineering, Shanghai Jiaotong University, 200240, Shanghai, China
- ^f Deepwater Engineering Research Centre, State Key Laboratory of Coastal and Offshore Engineering, Dalian University of Technology, Dalian, 116024, China

ARTICLE INFO

Keywords: Offshore wind turbine Single blade installation Underactuated system Backstepping control

ABSTRACT

The assembly and installation costs account for a large share in the overall expenditures of an offshore wind farm project. Single blade installation is suitable for large scale wind turbines due to the lower crane capability requirement and lower transportation time. By introducing active tension control on the tugger lines, an automatic single blade installation approach can accomplish operations in higher sea states, reduce the waiting-on-weather time, and improve the operational efficiency. Compared to early research, a more complicated control objective is achieved in this paper, i.e., a two-tugger-line configuration is applied to stabilize the suspended blade in three degrees of freedom during crane rotation and blade root-hub mating processes. The pulleys on the crane boom, i.e., the ends of the tugger lines, are assumed to be fixedly placed, resulting in tugger line time-varying inclinations. A novel backstepping-like controller is designed and proved. It is able to stabilize the blade around its equilibrium and make it track the desired path. Sensitivity studies are conducted to evaluate the influence of the tugger line inclinations. In addition, the influence of the installed blades on a three-blade horizontal wind turbine with a monopile foundation is discussed. The proposed active control setup improves the installation success rate and reduces the risks for blade impacts that may occur during mating.

1. Introduction

Wind energy is the fastest growing and most practical renewable energy source in the current market. Offshore wind turbines (OWTs) have received increased attention due to effective and stable electricity generation [1]. However, electric power produced by OWTs is more expensive compared to onshore wind, due to the enormous expenses of foundation structures and major components assembly and installation in the complicated offshore environment [2,3]. The assembly and installation cost occupies 19.0% of the overall expenditures for a bottom-fixed offshore wind turbine project [4,5], and it is expected to be even higher for floating offshore wind turbine projects [6,7]. Therefore, improving the OWT installation efficiency is important to enhance the market share of wind

E-mail address: zhenxingwei@dlut.edu.cn (X. Zhen).

^{*} Corresponding author.

energy [8]. Given the fact that bottom fixed projects are more predorminant, we focus on the bottom fixed wind turbine in this paper.

There are several OWT installation strategies according to the level of onshore preassembly [9]. One solution is to assemble the OWT onshore. From the port to wind farm, the preassembly can be towed by tugboats [10] or carried by a installation vessel [11]. This strategy shortens offshore operation period and improves the installation efficiency by reducing the operational complexity. Another strategy is to install piece by piece, for example the single blade installation approach, where each blade is lifted and installed to the hub individually. More components can be transported in one vessel by placing the parts closely on the deck, ensuring a higher deck utilization and demanding a lower crane capability. Therefore, this approach promotes shorter overall OWT units transportation time and allows a wider selection of crane vessels. The selection of installation strategy is a tradeoff of several considerations, such as system dynamics [12,13], risk analysis [14], environmental impacts [15], crane load analysis [16], and site selection [17,18]. Research on single blade installation focuses on modeling of dynamics, analysis of the mating success rate, and studies of the effects of impact between the blade guide pin and hub [19-24]. An optimized lifting controller is proposed in Ren et al. [21] using model predictive control theory. The criteria of the final mating period is studied in Jiang et al. [22] by numerical simulations. By applying the finite element method and simulations, the influence of the blade-hub impact is analyzed in Verma et al. [23]. To monitor the hub and blade motion, an accurate payload motion tracking algorithm is proposed based on sensor fusion in Maes et al. [24]. Ren et al. [20] proposes an automatic control system with actuation of two tugger lines to control the blade orientation in the horizontal plane (yaw) and motion in the direction perpendicular to the spanwise direction in the horizontal plane (surge), resulting in a fully-actuated system. However, motions in the other four degrees of freedom (DOFs) (including sway, heave, roll, and pitch), are not controllable and neglected. To overcome the need of pretension in Ren et al. [20], a three-tugger-line configuration is discussed in Ren et al. [25]. In Ren et al. [20] and Ren et al. [25], the automatic tugger line controllers can stabilize the suspended blade in a turbulent wind field, based on the assumptions that the direction of the tugger lines remains in the wind inflow direction, and that the crane tip is fixed in space, whereas the tugger line orientations do not always stay in parallel to the wind direction in practical applications. Moreover, the crane motion is also not considered as the crane tip is assumed to be fixed in space. Another weakness is that the control law can only mitigate the absolute blade motion, and not the relative motion partly contributed by the wave-and-wind-induced hub motion.

To overcome the above-mentioned drawbacks, the complexity of the automatic control scheme is significantly improved in this paper. The control objective is still to reduce the relative motion between the blade root center and hub. The major contributions and differences are summarized as follows.

- An underactuated scheme for the entire blade mating process is proposed, where a more practical two-tugger-line configuration is studied and three DOFs (surge, sway, and yaw) are controlled;
- The control law can achieve blade stabilization and root-hub tracking operations, but early control designs only can stabilizing the blade in the air;
- Crane rotation is firstly considered in the automated single blade installation scheme, while early research assumes the crane tip is fixed in space;
- The influence of the installed blades and tugger line placement are analyzed; however, the earlier studies only consider monopile foundation without installed blade and two tugger lines placed perpendicularly to the blade span without time-varying inclinations.

It aims to further increase the operational limits, improve mating success rate, enhance safety, and broaden the weather window and reduce the offshore installation time.

The paper is organized as follows. The mating problem and derivations of a control design model are introduced in Section 2, showing that this becomes an underactuated control problem. In Section 3, a controller is designed to handle the underactuated configuration using a backstepping-like technique, and the closed-loop system is proved stable by the direct Lyapunov method [26]. In addition, the motion planning algorithm is discussed. Simulation results of the proposed automatic installation scheme in all three stages are shown in Section 4. In Section 5, sensitivity studies are conducted to evaluate the influence of the tugger line inclinations caused by the pulley placement. The influence of the crane motion is also discussed.

2. Problem formulation

To maintain consistency, a well-studied single blade installation scheme [22] is taken as an example. The installation configuration and its simplified form are presented in Figs. 1–2. A monopile foundation has been hammered into the seabed. A jackup installation vessel carries the wind turbine units to the installation site. The jackup vessel is rigidly supported by jacking the legs into the seabed. Supporting structures, including the tower sections, nacelle, and hub have been bolted upwards subsequently on the foundation. A blade is seized by a yoke and lifted to the hub height by a boom crane through a lift wire. There are two tugger lines connecting the crane boom and yoke to constrain the blade pendular motion, which is induced by the turbulent wind field. A feedback-controlled winch servomotor connects each tugger line through a pulley, which is mounted on the crane boom and can move along the longitudinal direction, such that the winch is capable to control the tension force acting on the tugger line.

A wind turbine blade is made up of composite material and consists of several bolted connections at its root. These bolted connections are docked into the flange holes of the hub during a successful mating task. The entire process requires a very high precision, and therefore a few elongated bolts called 'guide pins' are used; see Fig. 3. The guide pins are structurally softer than the normal bolts and are temporarily attached to the root during mating. The primary goal of these pins is to assist the offshore

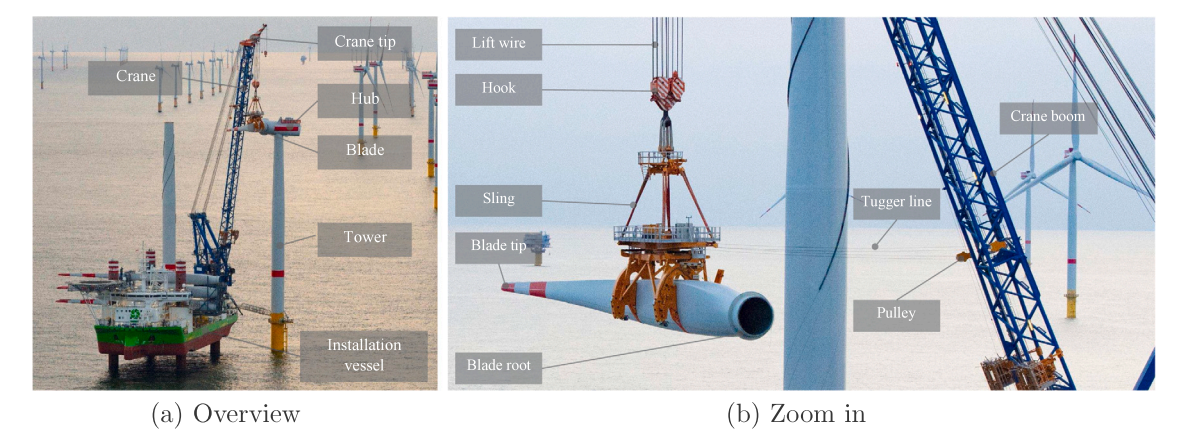


Fig. 1. Configuration of single blade installation [courtesy of DEME Group].

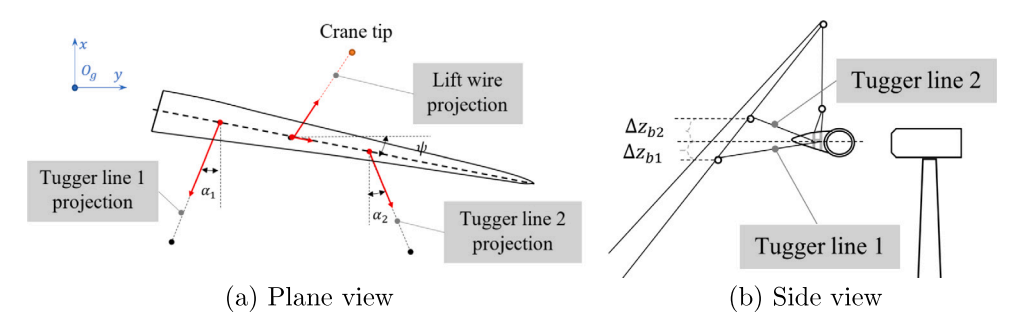


Fig. 2. Simplified diagram of single blade installation.

crew to visually track the relative motion between the blade root and hub, and to pull into the flange holes during the mating. The influence of the root-and-hub relative motions to the mating process are two-fold. First, the relative displacement between the blade root and hub influences the mating success rate [22]. In wind field with high mean wind speed, the motion of the guide pin can be too large to accurately plugin. In addition, a large displacement gives a higher possibility for large impact velocity, which can cause substantial impact forces between the guide pin and the hub. This can damage the sensitive root connections. In [23], it was found that the blade root suffers severe bending of the guide pin causing substantial damage to the root laminate. Such damages are critical from a structural design perspective because the blade root is designed to carry large torsional and bending loads during power production. If a mating attempt should fail due to the damaged guide pin, the blade must be hoisted back to the installation vessel. This leads to installation delays and loss of favorable weather windows for subsequent activities. Consequently, the root-and-hub relative motion during the mating process is a potential cause of delay or failure of the installation task, which must be avoided.

2.1. Proposed mating procedures

First, the blade is lifted from the deck by the crane [21]. There are three stages after lifting the blade to the hub height; see Fig. 4.

- Stage 1 (Stabilizing): Control the tension forces on the tugger lines to stabilize the suspended blade in the turbulent wind field;
- Stage 2 (Transportation): Control the crane to transport the blade to the mating position; meanwhile, control the tension forces on the tugger lines to keep the blade orientation as the planned trajectory, and stabilize the blade motion in the horizontal plane during the transportation.
- Stage 3 (Mating): Control the crane and tension forces on the tugger lines to track the hub motion, reduce the relative position and velocity between blade root and hub, and stabilize the blade orientation to ensure a successful mating operation.

Stage 1 is similar to the problem stated in [20], which uses a simplified configuration. To ensure an accurate mating operation, the states to be controlled are the blade-root positions, instead of the blade COG ones. The hub oscillation is dominated by the first eigenmode of the tower-monopile system, approximately $4 \, \text{s}$, while the blade pendular motion has a higher natural period about $10\text{--}12 \, \text{s}$.

Note that stages 2 and 3 are different from traditional procedures which heavily relay on manual work from the installation crew inside the hub.

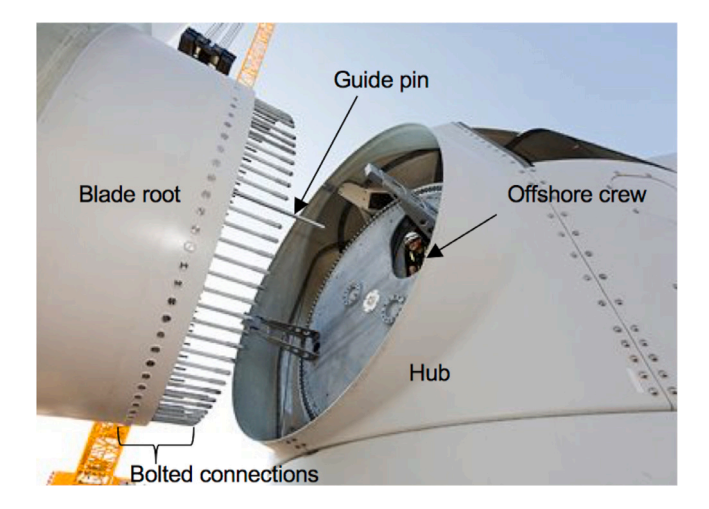


Fig. 3. A typical view of the mating process involving use of guide pin at blade root connection. Source: [27].

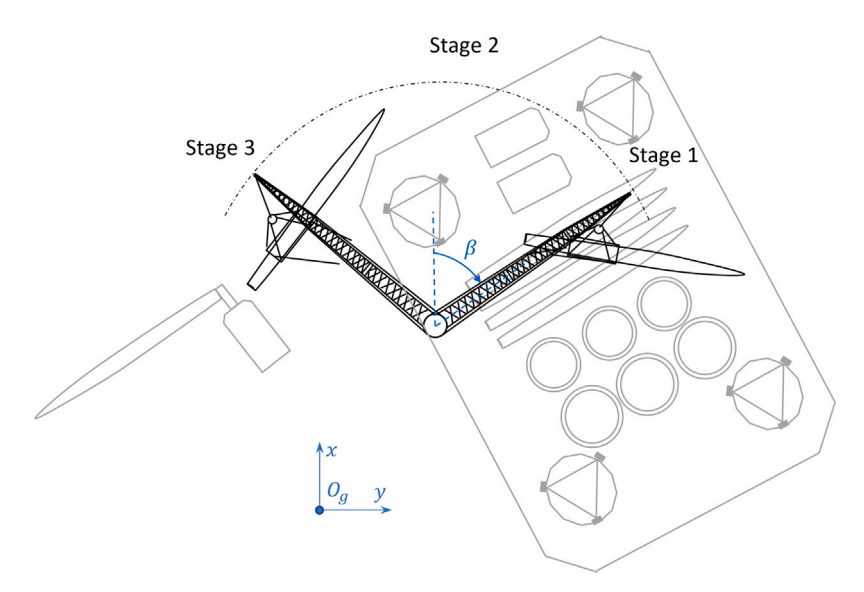


Fig. 4. Diagram of the three single blade installation stages.

2.2. Mating conditions

Since the wave-induced hub motion is a narrow-banded process and the natural period is determined by structural characteristics, the hub motion is dominated by the natural frequency of the tower's 1st fore-aft bending mode, which experiences a minor reduction as the number of the mounted blade increases. The amplitude depends on not only the structural stiffness but also the environmental parameters, especially, the significant wave height, wave period, wind direction, wind speed, and turbulence intensity (*TI*). Moreover, the hub motion is also influenced by the already installed blade units. For a three-blade horizontal-axis wind turbine, there are three mating conditions (MCs) for Stage 3, demonstrated in Fig. 5.

- MC1: The nacelle and hub have been assembled on the tower. The wind turbine yaw system rotates the nacelle to the mating direction, and the rotor is rotated to an orientation such that the selected flange face on the hub opposes the suspended blade root horizontally.
- MC2: After successfully bolting the first blade, the rotor rotates 120 deg to let the second flange face the mating orientation. The second blade is ready to be mated.
- MC3: Repeatedly, the rotor is rotated to horizontally align the third hub after bolting the second blade. The third blade is ready to conduct the mating operation.

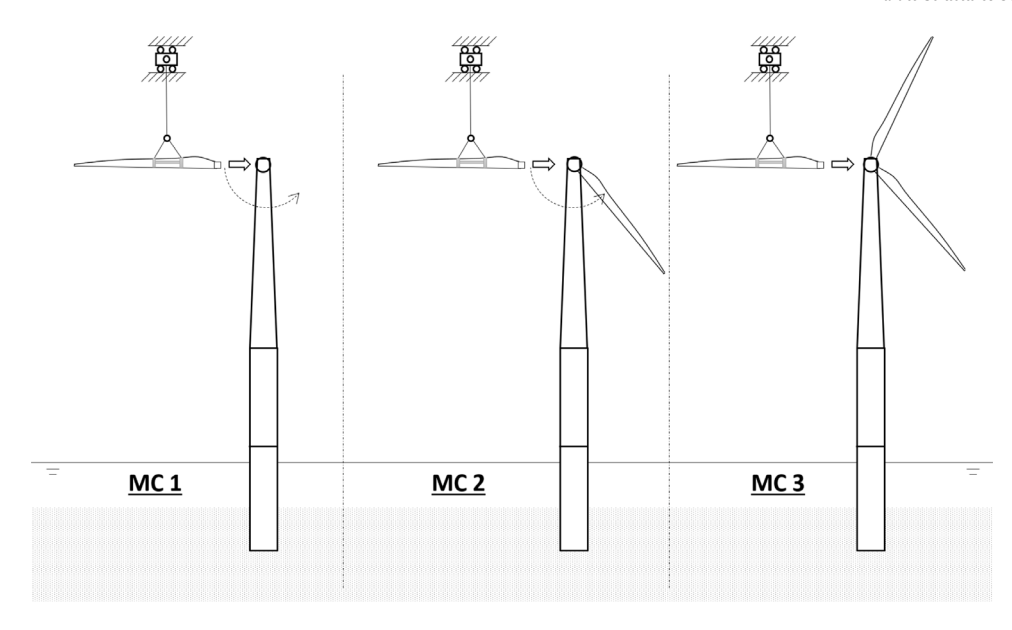


Fig. 5. Three monopile configurations before single blade installation.

Table 1
Structural and environmental parameters of the monopile OWT in the illustrative example.

Parameters	Unit	Value
Water depth	m	20
Mean wind speed U_w	m/s	10
Turbulence intensity TI	_	1.572
Wave spectrum	_	Pierson-Moskowitz
Significant wave height H_s	m	1.5
Wave period T_p	s	6
Pile length	m	36
Transition piece length	m	30
Tower length	m	77.6

Numerical comparative simulations are conducted to evaluate the influence to the natural period and spectrum peak resulting from the environmental loads and the pitch angles of the installed blades. The principal structural and environmental parameters are listed in Table 1. The water depth is 20 m, and turbulent wind field is adopted. In the simulations, the wind and waves comes from 0 deg to the wave direction, i.e., $\beta_w = 0$ deg and $\beta_{wave} = 0$, where β_{wave} is the statistic mean wave direction. The results are shown in Fig. 6.

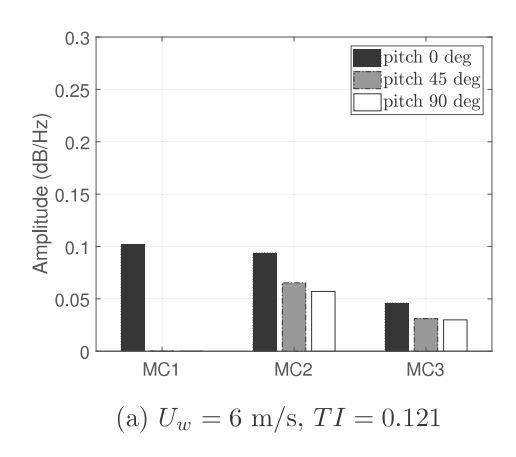
The first fore-aft natural frequencies are 0.258 Hz, 0.249 Hz, and 0.239 Hz for MC1, MC2, and MC3, respectively. For the NREL 5 MW reference wind turbine, each blade weighs 17 tonnes, which is considerably lower than the total mass without blade (1162 tonnes). Adding two blades slightly increases the total weight of the system, reduces the total stiffness, and slightly reduces the first fore-aft eigen-frequency from 0.258 Hz to 0.239 Hz. Though the eigenperiod moves towards the wave periods, blades have a damping characteristics, which increases with the number of installed blade and the blade pitch angle. Higher mean wind speed results in growing aerodynamic force; hence, the amplitude of the hub oscillation becomes larger. The pendulum motion of the blade has a dominant period of 10–12 s.

Some important observations are:

- The mated blades slightly influence the structural natural frequency.
- For MC1, the monopile motion is dominated by the wave-induced loads.
- For MC2 and MC3, the peaks of the amplitude spectra are smaller than that of MC1.
- · The peaks of the amplitude spectra decrease with increasing number and pitch angles of the installed blades.

2.3. System modeling

The entire system contains a single blade installation system and a monopile foundation. Two mathematical models are adopted to simulate the suspended blade in the MATLAB/Simulink environment, i.e., a simulation verification model (SVM) and a simplified control design model (CDM). The hub motions with specific environmental parameters and seeds are simulated in HAWC2 offline and imported to the MATLAB/Simulink environment. HAWC2 is an aeroelastic code developed by the DTU Wind Energy [28].



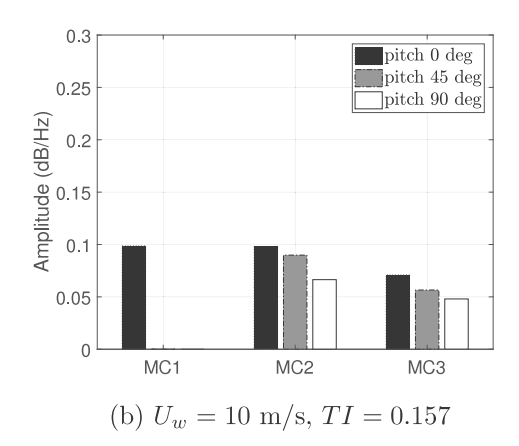


Fig. 6. Peaks of the amplitude motion spectrum in the wind direction in turbulence wind field with respective to the number and pitch angles of the installed blades, $\beta_{in} = 0$ and $\beta_{ivave} = 0$.

2.3.1. Simulation verification model

The SVM is built by the MarIn toolbox, a high-fidelity simulator for marine operations [19]. Modularized components are used to model the single blade installation process by Newton–Euler mechanics, containing a 3DOF hook, a 6DOF NREL 5 MW blade, a lift wire, two slings, and two tugger lines. Turbulent wind field is generated by the Mann's model [29]. The aerodynamic loads are calculated according to the cross-flow principle. The blade is modeled as a rigid body and its flexibility is negligible since the wind-induced deformation is very limited in low wind speed. The flexibility is less important for the root than for the tip. To avoid repetition, the interested reader is referred to Ren et al. [19] for detailed description of the methods.

2.3.2. Modeling of the foundation and installed blades

The monopile foundation, tower, and blades are modeled as Timoshenko beams in aeroelastic code HAWC2. From up to down, the soil under the seafloor are layered with different effective weights and angles of internal friction. Each layer is modeled as several springs with same stiffness which distributively support the corresponding segment of the foundation around the pile. The force acting on the pile is modeled as the superposition of the effects of several layers [30]. The wind loads on the pre-installed blades are calculated based on the steady lift and drag coefficients [31]. The pitch angles of the pre-installed blades are kept fixed during the simulations. Hence, the pitch angles are kept the same. The environmental loads are induced by the irregular waves and turbulent wind field. The history of the global hub motion is used as an input to the SVM.

2.3.3. Control design model

The CDM is a simplified 3DOF model for the purpose of designing control laws. The free-body diagram is presented in Fig. 7. Only the motions and forces in the horizontal plane are involved. There are three right-hand reference frames, i.e., the global NED system $\{n\}$, crane-fixed reference frame $\{c\}$, and blade body-fixed reference frame $\{b\}$.

- Global NED coordinate system $\{n\}$: The origin O_n is placed at the mean water level with the x- and y-axes pointing to the North and East, the z-axis pointing downward. The rotations about the x-, y-, and z-axes are named roll (ϕ) , pitch (θ) , and yaw (ψ) .
- Crane-fixed reference frame $\{c\}$: $\{c\}$ is a rotating frame in the horizontal plane. The origin O_c is laid at the projection of the crane boom center on the free sea surface. The x^c -axis points from O_c to the projection of the crane tip on the free sea surface. The z^c -axis heads downward. When O_n overlaps with O_c , $\{c\}$ is obtained by rotating $\{n\}$ with a crane boom angle β about the z^c -axis.
- Blade body-fixed reference frame $\{b\}$: The origin O_b is located at the blade center of gravity (COG). The y^b -axis points in the spanwise direction, from the root to tip. The z^b -axis accords to the edgewise direction, and the y^b -axis follows the right-hand rule The planar translational velocity components in $\{b\}$ are u, v, and w. The rotational velocity in yaw is denoted by r, respectively.

The CDM is introduced according to the following assumptions:

Assumption 1. The controller can stabilize the blade near the desired position and orientation, and the motion oscillation is not significant compared to the length of the tugger lines;

Assumption 2. The tugger lines are modeled as linear springs that provide positive restoring force in the direction from the blade yoke connecting point to the pulley on the boom;

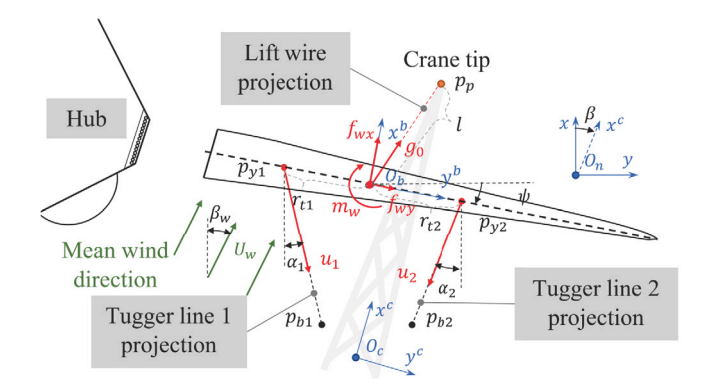


Fig. 7. Free body diagram of a single blade installation.

Assumption 3. The wind and wave directions do not significantly change during the installation.

A 3DOF simplified single blade installation model about the blade COG, proposed in [20], is modified by including the crane tip motion

$$\dot{p} = R_1(\psi)v^b \tag{1a}$$

$$\dot{\psi} = r$$
 (1b)

$$M\dot{v} = R(\psi)^{T}(g_0 + b + Bu_t) + \tau_{wt}$$
 (1c)

where $p := \operatorname{col}(x, y) \in \mathbb{R}^2$ denotes the position of the blade COG in the $\{n\}$, $\psi \in S^1$ is the yaw angle, $v^b \in \mathbb{R}^2$ refers to the linear velocity in $\{b\}$, $r \in \mathbb{R}$ is the yaw rate, $v := \operatorname{col}(v^b, r) \in \mathbb{R}^3$, $b := \operatorname{col}(b_1, b_2, b_3) \in \mathbb{R}^3$ is a state vector used to estimate the bias loads resulting from the model uncertainty and environmental disturbances. The transformation matrices $R \in SO(3)$ and $R_1 \in SO(2)$ from $\{b\}$ to $\{n\}$ are given by

$$R_1(\psi) := \begin{bmatrix} \cos \psi & -\sin \psi \\ \sin \psi & \cos \psi \end{bmatrix} \text{ and } R(\psi) := \begin{bmatrix} R_1(\psi) & \\ & 1 \end{bmatrix}. \tag{2}$$

Note that the rotation matrix R_1 in the horizontal plane satisfies

$$R_1^{-1} = R_1^{\mathsf{T}}, \ \dot{R}_1 = rR_1\bar{S}, \text{ where } \bar{S} := \begin{bmatrix} 0 & -1 \\ 1 & 0 \end{bmatrix}.$$
 (3)

 $M:=\operatorname{diag}(m,m,I_b)\in\mathbb{R}^{3 imes3}$ denotes the mass matrix of the system where $m=m_b+m_h+m_y$ is the total mass of the blade, hook, and yoke, I_b is the blade's moment of inertia at COG, $g_0:=[-\frac{mg}{l}(x-x_p),-\frac{mg}{l}(y-y_p),0]^{\mathsf{T}}$ represents the gravity-induced restoring force where $I=\sqrt{(x-x_p)^2+(y-y_p)^2}$ is the projection distance between the crane tip and the blade COG in xy-plane, the position of the crane tip in the horizontal plane is $p_p=[x_p,y_p]^{\mathsf{T}}$, and $u_t:=[u_1,\ldots,u_N]^{\mathsf{T}}\in\mathbb{R}^N$ is the control input vector, where N is the total number of tugger lines and $u_i\in\mathbb{R}$ is the ith tugger line horizontal force input, with $i=1,\ldots,N$. By introducing pretension, which is generated by gravity due to the blade initial displacement, u_i can be both positive and negative. In order to transfer the tugger line force inputs to the generalized control load acting on the blade in $\{n\}$, a general form of control configuration matrix B is given by

$$B(\alpha_1, \dots, \alpha_N) := \begin{bmatrix} B_1(\alpha_1) & \cdots & B_N(\alpha_N) \end{bmatrix}, \tag{4}$$

where $B_i(\alpha_i) := [-\cos \alpha_i, -\sin \alpha_i, r_{ti}\cos \alpha_i\cos \psi]^{\mathsf{T}}$, r_{ti} is the moment arm of the tugger line force u_i w.r.t. the COG in y^b , and α_i is the tugger line inclination in the horizontal plane.

In our case, N=2, $r_{t1}<0$, and $r_{t2}>0$. By Assumption 1, the angle α_i is considered to be unchanged in a short interval, i.e., $\dot{\alpha}_1=\dot{\alpha}_2\approxeq0$ and

$$\alpha_i = \sin^{-1}\left(\frac{y_{yi} - y_{bi}}{l_{ti}}\right), \quad i = 1, 2.$$

$$(5)$$

The sign of α_i depends on r_{ti} and the diameter of the crane boom. The wind-induced force in the body-fixed reference frame at an airfoil segment depends on the inflow velocity relative to the blade segment at y^b , given by $u^b_{uv}(y^b) = u^b_w - u^b_b(y^b)$, where $u^b_w = [U_w \cos(\psi - \beta_w), U_w \sin(\psi - \beta_w), 0]^{\mathsf{T}} \in \mathbb{R}^3$ is the wind velocity in $\{b\}$, $U_w \in \mathbb{R}$ and $\beta_w \in \mathbb{R}$ are the mean wind speed and direction, and $u^b_b(y^b)$ is the velocity at the corresponding blade segment center of pressure at y^b . Assumption 3 meets the cross-flow principle. According to the cross-flow principle and neglecting the blade velocity, i.e., $u^b_b(y^b) = 0$, the wind loads acting on the blade

COG in $\{b\}$ is simplified to the following form

$$\tau_{w} = \begin{bmatrix} f_{wx} \\ f_{wy} \\ m_{w} \end{bmatrix} = \begin{bmatrix} c_{wx} U_{w}^{2} \cos^{2}(\psi - \beta_{w}) \\ 0 \\ c_{w\psi} U_{w}^{2} \cos^{2}(\psi - \beta_{w}) \end{bmatrix}, \tag{6}$$

where c_{wx} and $c_{w\psi}$ are the generalized aerodynamic coefficients from the curve fitting of quasi-steady analysis results in surge and yaw, respectively. For the sake of simplification, $\beta_w = 0$ is used in this paper, i.e., the mean wind velocity vector is $u_w = [U_w, 0, 0]^{\mathsf{T}}$ in $\{n\}$. The turbulent wind speed is considered as a zero-mean system disturbance.

The global positions of the tugger line connecting points to the crane boom and yoke are $p_{bi} = [x_{bi}, y_{bi}, z_{bi}]^{\mathsf{T}}$ and $p_{yi} = [x_{yi}, y_{yi}, z_{yi}]^{\mathsf{T}}$, where $i \in \{1, 2\}$ is the index of the tugger lines. The position of the crane tip pulley is $p_p = [x_p, y_p, z_p]^{\mathsf{T}}$. Due to the vertical displacement of the pulley, the positions of the tugger line base points (pulleys) are given by

$$p_{bi} = p_{O_b} + \begin{bmatrix} R_1(\psi) \begin{bmatrix} 0 \\ r_{ti} \end{bmatrix} + R_1(\alpha_i) \begin{bmatrix} -l_{ti} \\ 0 \end{bmatrix} \end{bmatrix} + \begin{bmatrix} 0 \\ 0 \\ \Delta z_{bi} \end{bmatrix}, \tag{7}$$

where p_{O_b} is the position of O_b in $\{n\}$, l_{ii} denotes the tugger line length, and Δz_{bi} is the pulley's vertical displacement. We make the following assumptions for the control design:

Assumption 4. The crane tip moves in the horizontal plane without any vertical motion.

Assumption 5. The state b can be well estimated by the observer and compensated directly based on the estimate.

Assumption 6. The yaw angular rate $\dot{\psi}$ is small.

The vector relative degree of system (1) is [2,2]. Transfer system (1) to $\{n\}$ by applying the relation in (3). A new state is defined as $v = \dot{p} \in \mathbb{R}^2$. Then, the dynamics (1) can be compactly written as

$$\dot{p} = v$$
 (8a)

$$\dot{\psi} = r$$
 (8b)

$$\dot{v} = f_1(p, \psi, v, r) + G_1(p, \psi)u_t + d_1 \tag{8c}$$

$$\dot{r} = f_{\gamma}(p, \psi, v, r) + g_{\gamma}^{\mathsf{T}}(p, \psi)u_{t} + d_{\gamma},$$
 (8d)

where $d_1 \in \mathbb{R}^2$ and $d_2 \in \mathbb{R}$ are modeled as zero-mean process disturbances caused by the difference between the real wind-induced loads and the values calculated from the curve fitting, $f_1(p,\psi,v,r): \mathbb{R}^2 \times \mathcal{S}^1 \times \mathbb{R}^2 \times \mathbb{R} \mapsto \mathbb{R}^2$ and $f_2(p,\psi,v,r): \mathbb{R}^2 \times \mathcal{S}^1 \times \mathbb{R}^2 \times \mathbb{R} \mapsto \mathbb{R}$ are nonlinear functions, $G_1(p,\psi): \mathbb{R}^2 \times \mathcal{S}^1 \mapsto \mathbb{R}^{2\times 2}$, and $g_2(p,\psi): \mathbb{R}^2 \times \mathcal{S}^1 \mapsto \mathbb{R}^2$, i.e.,

$$f_1 = \bar{S}vr + \bar{G}(p - p_p) + \frac{1}{m}(\tau_{wn1} + b_1), \tag{8e}$$

$$G_1 = \bar{B}_1, \tag{8f}$$

$$f_2 = \frac{1}{I}(\tau_{wn2} + b_2),\tag{8g}$$

$$g_2^{\mathsf{T}} = \cos \psi \, \bar{B}_2,\tag{8h}$$

$$\tau_{wn1} = c_{wx} U_w^2 \cos^2(\psi - \beta_w) \begin{bmatrix} \cos \psi \\ \sin \psi \end{bmatrix}, \tag{8i}$$

$$\tau_{um^2} = c_{uvu} U_w^2 \cos^2(\psi - \beta_w),$$
 (8j)

where the bar operator denotes constant matrices for $\bar{B}_1 := \frac{1}{m} \begin{bmatrix} -\cos\alpha_1 & -\cos\alpha_2 \\ -\sin\alpha_1 & -\sin\alpha_2 \end{bmatrix}$, $\bar{B}_2 := \frac{1}{I} [r_{t1}\cos\alpha_1, r_{t2}\cos\alpha_2]$, and $\bar{G} := -\frac{g}{I} I_{2\times 2}$. Assumption 1 and Assumption 6 justify that the matrices \bar{B}_1 and \bar{B}_2 can be considered as constant.

2.4. Problem statement

The mating criteria are the relative position and velocity between the blade root center and hub, as well as the orientation disparity between the blade and mating flange [22,23]. The length of the lift wire is adjusted to stabilize the blade root at the mating height. To realize a successful mating operation from a height near the hub, the following criteria are of significance:

- The outcrossing rate of the in-plane projected relative distance between blade root center and hub is limited within an accepted circular boundary [22].
- The impact speed, relative out-plane velocity between the blade root and hub, is limited to prevent damaging the guide pins [23].
- · The blade root side faces the hub mating flange, which guarantees the guide pins a successful plugging.

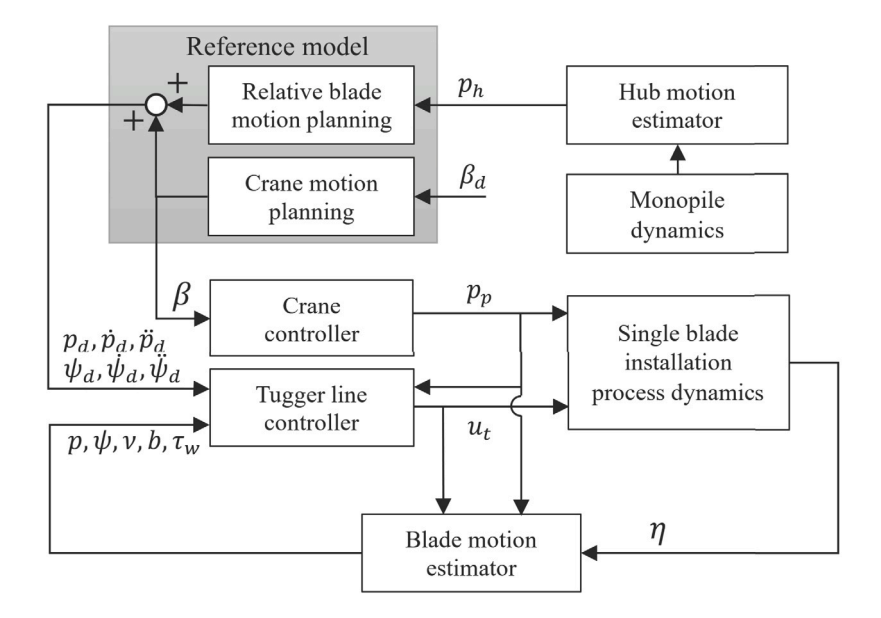


Fig. 8. Block diagram of the proposed active control scheme for single blade installation. The hat operator (*) denotes the estimates from observer.

MC1 is considered for the control problem hereafter. In Stage 1, the control objective is to stabilize the blade against the wind-induced loads, defined as a regulation control problem. In Stage 3, the control objectives considered in this paper are to design a control law to minimize the relative motion between the blade root center and hub and to keep an acceptable orientation, thus considered as a tracking control problem. The control inputs are the crane horizontal motion and the tension on the tugger lines.

The block diagram is presented in Fig. 8. The OWT foundation and blade motions are sampled by sensors, such as Global Navigation Satellite System (GNSS) and inertial measurement unit (IMU). The observer filters the measurement noise and fuses various measurements to achieve a precise motion estimate of the monopile hub and suspended blade, e.g., position, velocity, and acceleration; details can be found in [20,24,32]. The reference model contains two modules, i.e., the crane motion planning module and relative blade motion planning module. The crane motion planning module outputs the rotational trajectory for the crane boom to transport the blade from the deck to the installation site near the hub. The relative blade motion planning module generates real-time trajectories for the blade root, according to the crane operation and hub motion from the hub motion estimator. Utilizing the estimate from observers and the designed trajectories, the actuators control the crane and tugger lines to realize the control objective.

Assumption 7. Since the emphasis of this paper is on the development of the control law and its performance evaluation, an observer design is not considered. Hence, full-state feedback is assumed available. In practice, feedback is provided by some state estimator module that filters the measurements and reconstructs unmeasured states.

The position of the root center in $\{b\}$ is $[x_r^b, y_r^b, z_r^b]^{\mathsf{T}}$. Defining $l_r = \operatorname{col}(x_r^b, y_r^b)$ as the distance vector from the blade COG to root center, the root position in $\{n\}$ becomes

$$q := p + R_1(\psi)l_r. \tag{9}$$

Let $q_d: \mathbb{R}_{\geq 0} \mapsto \mathbb{R}^2$ and $\psi_d: \mathbb{R}_{\geq 0} \mapsto S^1$ be C^2 desired position and orientation time signals for the blade root, generated by a reference system. The control objective is then to design a feedback control law that stabilizes the closed-loop system and makes the tracking errors converge to zero, i.e., for $\tilde{q}:=q-q_d(t)$ and $\tilde{\psi}:=\psi-\psi_d(t)$ we aim for $(\tilde{q}(t),\tilde{\psi}(t))\to 0$ as $t\to\infty$.

3. Control design

The proposed single blade installation system is an underactuated system, where the motions in three DOFs $(x, y, \text{ and } \psi)$ are the objectives of control with only two available control inputs $(u_1 \text{ and } u_2)$.

Given the references $q_d(t)$, $\psi_d(t)$, and their time derivatives, let

$$p_d(t) := q_d(t) - R_1(\psi_d(t))l_r, \tag{10}$$

$$v_d(t) := \dot{p}_d(t),\tag{11}$$

$$r_d(t) := \dot{\psi}_d(t),\tag{12}$$

and let $\tilde{p} := p - p_d(t)$, $\tilde{v} := v - v_d(t)$, $\tilde{\psi} := \psi - \psi_d(t)$, and $\tilde{r} := r - r_d(t)$. The resulting error state equation becomes

$$\dot{\tilde{p}} = \tilde{v},$$
 (13a)

$$\dot{\bar{\psi}} = \tilde{r},\tag{13b}$$

$$\dot{\tilde{v}} = f_1(p, \psi, v, r) + G_1(p, \psi)\alpha(p, \psi, v, r, t) - \dot{v}_d(t), \tag{13c}$$

$$\dot{\tilde{r}} = f_{\gamma}(p, \psi, v, r) + g_{\gamma}^{\mathsf{T}}(p, \psi)\alpha(p, \psi, v, r, t) - \dot{r}_{d}(t). \tag{13d}$$

where α is the virtual control law to be designed.

The control objective is then equivalent to rendering the closed-loop system stable and ensuring convergence to an equivalent point which is closed to $(\tilde{p}, \tilde{v}, \tilde{\psi}, \tilde{r}) = 0$.

3.1. Control design 1: Transverse position and orientation

We first only consider the problem of controlling the transverse dynamics and orientation, that is, making $x(t) \to x_d(t)$ and $\psi(t) \to \psi_d(t)$ as $t \to \infty$. This avoids an underactuated design, since we control two DOFs by two control inputs. According to feedback linearization, the controller proposed in [20] can be adopted, i.e.,

$$u_t = -(LM^{-1}B)^{-1} \left[L \left(RS(r)v + M^{-1}(g_0 + b) + RM^{-1}\tau_w \right) - [\ddot{p}_d, \ddot{\psi}_d]^{\mathsf{T}} - u_{pid} \right], \tag{14}$$

where $L = \begin{bmatrix} 1 & 0 & 0 \\ 0 & 0 & 1 \end{bmatrix}$, $S(r) = \begin{bmatrix} \bar{S}r & 0 \\ 0 & 0 \end{bmatrix}$, and

$$u_{pid} = -K_p \begin{bmatrix} x - x_d \\ \psi - \psi_d \end{bmatrix} - K_d \begin{bmatrix} \dot{x} - \dot{x}_d \\ \dot{\psi} - \dot{\psi}_d \end{bmatrix} - K_i \int \begin{bmatrix} x - x_d \\ \psi - \psi_d \end{bmatrix} \, dt.$$

where gains K_n , K_i , and K_d are selected using the pole-placement technique.

The difference with [20] is the matrix B, which is caused by the tugger line inclination α_1 and α_2 . The force component in the longitudinal direction is not well controlled. When the desired yaw angle ψ_d is away from zero, the amplitude of the motion in the x-direction can be large due to the tugger line inclinations. Hence, a more advanced control algorithm is presented.

3.2. Control design 2: Underactuated control of position and orientation

For the design of the control law, we assume $(d_1, d_2) = 0$, and use a backstepping-like design, including integral action [33,34]. Instead of directly designing the virtual controller to cancel the error dynamics, a new error state z_1 is designed.

Step 1: Since the system is underactuated, we define the first error state $z_1 \in \mathbb{R}^2$ as a combination of the linear and angular tracking errors, according to

$$z_{1} = \tilde{p} + K \left[\tilde{\psi} + \tilde{r} - \cos \psi \bar{B}_{2} \bar{B}_{1}^{-1} \tilde{v} \right]$$

$$= (p - p_{d}(t)) + K \left[\tilde{\psi} + \tilde{r} - \cos \psi \bar{B}_{2} \bar{B}_{1}^{-1} (v - \dot{p}_{d}(t)) \right],$$
(15)

where $K := \operatorname{col}(k_1, k_2) \in \mathbb{R}^2$ is a constant gain vector to be tuned. Rendering $z_1 = 0$ will then ensure that the equilibrium point $(\tilde{p}^*, \tilde{\psi}^*, \tilde{v}^*, \tilde{r}^*)$ stays close to the origin. The error dynamics is now given by

$$\begin{split} \dot{z}_{1} &= v - v_{d} + K[\tilde{r} + \dot{r} - \dot{r}_{d} - \cos\psi \bar{B}_{2} \bar{B}_{1}^{-1} (\dot{v} - \dot{v}_{d}) + r \sin\psi \bar{B}_{2} \bar{B}_{1}^{-1} (v - \dot{p}_{d})] \\ &= v - v_{d} + K[\tilde{r} + f_{2} + g_{2}^{\mathsf{T}} u_{t} - \dot{r}_{d} - \cos\psi \bar{B}_{2} \bar{B}_{1}^{-1} (f_{1} + G_{1} u_{t} - \dot{v}_{d}) + r \sin\psi \bar{B}_{2} \bar{B}_{1}^{-1} \tilde{v}] \\ &= v - v_{d} + K[\tilde{r} + f_{2} - \dot{r}_{d} - \cos\psi \bar{B}_{2} \bar{B}_{1}^{-1} (f_{1} - \dot{v}_{d}) + r \sin\psi \bar{B}_{2} \bar{B}_{1}^{-1} \tilde{v}], \end{split}$$

$$(16)$$

where the control input u_t was canceled since $g_2^\top = \cos\psi \bar{B}_2 \bar{B}_1^{-1} G_1$. We consider v as a control input in (16), let $\vartheta_1 \in \mathbb{R}^2$ be a corresponding virtual control, and define $z_2 := v - \vartheta_1 \in \mathbb{R}^2$ as the error between v and the virtual control. To also include integral action, let

$$z_0 := \int_0^t z_1(\sigma) d\sigma. \tag{17}$$

We then define the Step 1 control Lyapunov function (CLF) of the backstepping design [26,35], $V_1 = \frac{1}{2}z_0^T C_0 z_0 + \frac{1}{2}z_1^T z_1$, $C_0 = C_0^T > 0$, which together with the virtual control

$$\vartheta_1 = -C_0 z_0 - C_1 z_1 + v_d - K \left[\tilde{r} + f_2 - \dot{r}_d - \cos \psi \, \bar{B}_2 \bar{B}_1^{-1} (f_1 - \dot{v}_d) + r \sin \psi \, \bar{B}_2 \bar{B}_1^{-1} \tilde{v} \right], \tag{18}$$

and $C_1 = C_1^{\top} > 0$, yields

$$\dot{V}_1 = -z_1^{\mathsf{T}} C_1 z_1 + z_1^{\mathsf{T}} z_2,\tag{19a}$$

$$\dot{z}_0 = z_1,\tag{19b}$$

$$\dot{z}_1 = -C_0 z_0 - C_1 z_1 + z_2,\tag{19c}$$

Fig. 9. Diagram of the cascade system.

For $z_2 = 0$, the subsystem (\dot{z}_0, \dot{z}_1) is a linear autonomous system that is UGES.

Step 2: Differentiating z_2 yields

$$\dot{z}_2 = \dot{v} - \dot{\theta}_1 = f_1 + G_1 u_t - f_A - G_A u_t = (f_1 - f_A) + (G_1 - G_A) u_t, \tag{20}$$

where $\theta_1 = f_4 + G_4 u_t$ are elaborated in Appendix A. Defining the Step 2 control Lyapunov function, $V_2 := V_1 + \frac{1}{2} z_1^T z_2$, yields

$$\dot{V}_{2} = -z_{1}^{T}C_{1}z_{1} + z_{2}^{T}(z_{1} + \dot{z}_{2}) = -z_{1}^{T}C_{1}z_{1} + z_{2}^{T}[z_{1} + (f_{1} - f_{4}) + (G_{1} - G_{4})u_{t}]. \tag{21}$$

The feedback control law is now chosen as

$$u_t = \alpha(p, \psi, v, r, t) = (G_1 - G_4)^{-1} (-z_1 - f_1 + f_4 - C_2 z_2), \tag{22}$$

where $C_2 = C_2^{\top} > 0$ is a diagonal gain matrix. This results in

$$\dot{V}_2 = -z_1^{\mathsf{T}} C_1 z_1 - z_2^{\mathsf{T}} C_2 z_2 \tag{23}$$

$$\dot{z}_2 = -z_1 - C_2 z_2. \tag{24}$$

Closed-loop system: Since the original system (8) is of dimension 6, and adding the integral state $z_0 \in \mathbb{R}^2$, the overall state space is of dimension 8. This implies an internal dynamics of dimension 2, where the closed-loop system can be represented by a cascade between the dynamics of $z = \operatorname{col}(z_0, z_1, z_2)$ and the internal dynamics; see Fig. 9.

The closed-loop equations in the z-dynamics, (19b), (19c), (24), have the global equilibrium $z_0 = z_1 = z_2 = 0$. Considering the closed-loop error equations in the original coordinates (13), we find that $\dot{\tilde{p}} = \tilde{v} = \dot{\tilde{v}} = 0$ and $\dot{\tilde{\psi}} = \tilde{r} = \dot{\tilde{r}} = 0$ must characterize the equilibrium. In this equilibrium, we get the constraints

$$\begin{split} &\vartheta_{1}|_{eq} = -C_{0}z_{0} - C_{1}z_{1} + v_{d} - K\left[\tilde{r} + f_{2} - \dot{r}_{d} - \cos\psi\bar{B}_{2}\bar{B}_{1}^{-1}(f_{1} - \dot{v}_{d}) + r\sin\psi\bar{B}_{2}\bar{B}_{1}^{-1}\tilde{v}\right] \\ &= v_{d} - K\left[\dot{r} - \dot{r}_{d} - g_{2}^{\top}\alpha - \cos\psi\bar{B}_{2}\bar{B}_{1}^{-1}(\dot{v} - \dot{v}_{d} - G_{1}\alpha)\right] = v_{d}, \\ &z_{1}|_{eq} = \tilde{p} + K\left[\tilde{\psi} + \tilde{r} - \cos\psi\bar{B}_{2}\bar{B}_{1}^{-1}\tilde{v}\right] = \tilde{p} + K\tilde{\psi} = 0, \\ &z_{2}|_{eq} = v - \vartheta_{1}|_{eq} = \tilde{v} = 0, \\ &G_{1} = \bar{B}_{1}, \qquad g_{2}^{\top} = \cos\psi\bar{B}_{2}, \qquad G_{3}|_{eq} = \bar{S}\left[\bar{B}_{1}r_{d} + v_{d}\cos\psi\bar{B}_{2}\right], \\ &G_{4}|_{eq} = -K\left[g_{2}^{\top} - g_{2}^{\top}\bar{B}_{1}^{-1}G_{3} + \sin\psi\bar{B}_{2}\bar{B}_{1}^{-1}G_{1} + \sin\psi\bar{B}_{2}\bar{B}_{1}^{-1}\tilde{v}g_{2}^{\top}\right], \\ &= -K\left[(\cos\psi + \sin\psi)\bar{B}_{2} - \cos\psi\bar{B}_{2}\bar{B}_{1}^{-1}\bar{S}\bar{B}_{1}r_{d} - \cos^{2}\psi\bar{B}_{2}\bar{B}_{1}^{-1}\bar{S}v_{d}\bar{B}_{2}\right], \\ &f_{1}|_{eq} = \bar{S}v_{d}r_{d} + \bar{G}(p - p_{p}) + \frac{1}{m}(\tau_{wn1} + b_{1}), \\ &\alpha|_{ea} = -\left(G_{1} - G_{4}\right)^{-1}\left(f_{1} - f_{4}\right). \end{split}$$

Substituting these constraints into (13), we have a non-zero equilibrium point $(\tilde{p}^*, \tilde{\psi}^*, \tilde{v}^*, \tilde{r}^*)$, which is a function of the external wind loads (τ_w) and $(p_g(t))$, crane tip motion $(p_g(t))$ and its derivatives), and reference signal $(p_d(t))$, $(p_d(t))$, and their derivatives).

Theorem 1. For the system (8), if $d_1 = d_2 = 0$ and Assumptions 4–6 hold, the control law (22) will guarantee trajectory tracking performance and the error dynamics (25) is uniformly globally asymptotically stabilize at its equilibrium point by well-tuned coefficients in K.

Proof. After introducing the reduce-order error state z_1 , the relative degree of the new system is less than that of (8). In the perspective of feedback linearization, the system is a cascade system with an external system and an internal system; see Fig. 9. After substituting the control law (22), the resultant external dynamics is

$$\dot{z}_0 = z_1,\tag{25a}$$

$$\dot{z}_1 = -C_1 z_1 - C_0 z_0 + z_2,\tag{25b}$$

$$\dot{z}_2 = -z_1 - C_2 z_2. \tag{25c}$$

The input and output are u_t and z_1 respectively. Substitute (25) into the CLF V_2 , the time derivative is

$$\dot{V}_2 = z_0^{\mathsf{T}} C_0 z_1 + z_1^{\mathsf{T}} (-C_1 z_1 - C_0 z_0 + z_2) + z_2^{\mathsf{T}} (-z_1 - C_2 z_2) = -z_1^{\mathsf{T}} C_1 z_1 - z_2^{\mathsf{T}} C_2 z_2 \le 0. \tag{26}$$

The invariant set is $z_0 \equiv 0$, $z_1 \equiv z_2 \equiv 0$. Applying Krasovskii–LaSalle's invariance principle, no solution can stay in $\dot{V} = 0$, other than the trivial solution $\text{col}(z_0, z_1, z_2) = 0$. Therefore, the system (25) is globally asymptotically stable at its origin $z_1 = z_2 = 0$.

As mentioned, $(\tilde{p}, \tilde{v}, \tilde{\psi}, \tilde{r}) = 0$ is not the equilibrium point of (13). Since $z_1 = \dot{z}_1 = \dot{z}_1 = 0 \in \mathbb{R}^2$, the equilibrium point of (13) can be found at $(\tilde{p}^*, \tilde{\psi}^*, \tilde{v}^*, \tilde{r}^*)$ by substituting the control law (22) and algebraic manipulations. Define $e_1 := [\tilde{p}, \tilde{\psi}]^{\mathsf{T}} - [\tilde{p}^*, \tilde{\psi}^*]^{\mathsf{T}}$ and $e_2 := [\tilde{p}, \tilde{r}]^{\mathsf{T}} - [\tilde{p}^*, \tilde{r}^*]^{\mathsf{T}}$. The internal system is then selected as

$$\dot{e}_1 = e_2, \tag{27a}$$

$$\dot{e}_2 = h(\tilde{p}, \tilde{v}, \tilde{\psi}, \tilde{r})|_{(\tilde{p}^*, \tilde{w}^*, \tilde{p}^*, \tilde{r}^*)}. \tag{27b}$$

The input and output are z_1 and e_1 , respectively. Therefore the whole system is global asymptotically stable at the equilibrium point with control law (22) such that the coefficients in matrix K is tuned to asymptotically stabilize the zeros dynamics (27).

Remark 1. The control law (22) depends the fact that $G_1 - G_4$ is invertible. The determinant of \bar{B}_1 is $\det(\bar{B}_1) = \frac{1}{m^2} \sin(\alpha_2 - \alpha_1)$. When α_1 is close to α_2 , \bar{B}_1^{-1} will be very large, resulting in instability.

Remark 2. Compared to the system proposed in [33], system (1) cannot satisfy $f_1(0,0) = 0$ and $f_2(0,0) = 0$ owing to the external wind-induced loads and pretension. The equilibrium point $(\tilde{p}^*, \tilde{\psi}^*, \tilde{v}^*, \tilde{r}^*)$ means the offset of the position and orientation between the desired trajectory and actual performance. Furthermore, the equilibrium point is determined by the selection of K, which assigns different weights to \tilde{p} and $\tilde{\psi}$. Hence, tuning coefficient matrix K is necessary. The tuning process balances several aspects, e.g., the capability to overcome the influence by d_1 and d_2 , tracking speed, position and orientation offset due to the equilibrium point, etc.

Remark 3. Since ψ only exists in G_1 and g_2 in a form of trigonometric functions, only local stability is guaranteed. The system performance is unchanged when the blade is rotated for a round 2π . Consequently, the equilibrium points appear periodically. However, this is not allowed in practical operations.

Remark 4. Theorem 1 is proven according to assumption $d_1 = 0$ and $d_2 = 0$. However, the system possibly become unstable resulting from d_1 , d_2 , and tugger line inclinations.

3.3. Reference model

In this paper, the only parameter for the crane is the boom angle β ; see Fig. 4. Since it is difficult to have accurate crane control, the crane is only used to transport the suspended blade from deck to hub.

Similar to the reference model proposed in [20], a three-order reference model is used in this paper. For the tugger line tension force control, crane control is an openloop process. The reference model generates real-time trajectories $(p_d(t), \psi_d(t))$ and its derivatives to the controller. The vector of the desired blade COG position and orientation is

$$r_{d}(t) = \begin{cases} \operatorname{col}([x_{O_{c}}, y_{O_{c}}]^{\mathsf{T}} + R_{1}(\beta)l_{c} + d_{pr} - R_{1}(\psi_{d})l_{r}, \psi_{d}), & \text{Stage 1,} \\ \operatorname{col}([x_{O_{c}}, y_{O_{c}}]^{\mathsf{T}} + R_{1}(\beta(t))l_{c} + d_{pr} - R_{1}(\psi_{d}(t))l_{r}, \psi_{d}(t)), & \text{Stage 2,} \\ \operatorname{col}(p_{h}(t) - R_{1}(\psi_{d})l_{r}, \psi_{d}), & \text{Stage 3,} \end{cases}$$

where $l_c \in \mathbb{R}^2$ is the distance vector between the crane tip projection to O_c on the horizontal plane, p_h is the position of the hub mating flange, and $d_{pr} = [x_r - x_p, y_r - y_p]^{\mathsf{T}}$ is the relative distance vector between the blade root and crane tip. Vector d_{pr} is constant in Stage 1 and Stage 2.

Continuous and smooth trajectories are planned between the initial and final values to achieve a smooth control towards the final desired position and orientation. A third-order filter is adopted as the reference model, which is given by

$$\begin{bmatrix} p_d \\ \psi_d \end{bmatrix}^{(3)} + (2\Delta_r + I)\Omega_r \begin{bmatrix} \ddot{p}_d \\ \ddot{\psi}_d \end{bmatrix} + (2\Delta_r + I)\Omega_r^2 \begin{bmatrix} \dot{p}_d \\ \dot{\psi}_d \end{bmatrix} + \Omega_r^3 \begin{bmatrix} p_d \\ \psi_d \end{bmatrix} = \Omega_r^3 r_d, \tag{29}$$

where $r_d \in \mathbb{R}^2 \times \mathbb{S}$ is the final setpoint position and orientation, $\Delta_r = \operatorname{diag}\{\zeta_1, \zeta_2, \zeta_3\} = \operatorname{diag}\{1, 1, 1\}$ and $\Omega_r = \operatorname{diag}\{\omega_{n1}, \omega_{n2}, \omega_{n3}\}$ are the matrices of relative damping ratios and natural frequencies in the reference model, respectively. The parameters ω_{n1}, ω_{n2} , and ω_{n3} should be tuned feasibly to the dynamic model. The third-order filter ensures the smoothness of signals \ddot{p}_a and $\ddot{\psi}_d$, which are used in $\dot{\theta}_1$ (Eq. (20)).

Similarly, the crane boom angle is also the output from a third-order filter, i.e.,

$$\beta^{(3)} + (2\zeta_{\beta} + 1)\omega_{\beta}\ddot{\beta} + (2\zeta_{\beta} + 1)\omega_{\beta}^{2}\dot{\beta} + \omega_{\beta}^{3}\beta = \omega_{\beta}^{3}\beta_{d}, \tag{30}$$

where $\zeta_{\beta}=1$ and ω_{β} are the relative damping ratio and natural frequency, respectively.

The hub motion is fast; however, the simulation results show that the system is not stable with fast crane rotation. Hence, values of ω_{β} for crane tip motion should be small, but values in Ω_r for hub motion should be larger. The crane only moves in Stage 2. The tugger lines are activated in all the mating processes. The activation of the crane and tugger lines is tabulated in Table 2.

Table 2
Activation and selection of parameters of the crane and tugger lines in stages 1–3.

	Stage 1	Stage 2	Stage 3
Tugger line	Yes	Yes	Yes
Natural frequency of (29) Ω_r	-	-	Fast
Crane	No	Yes	No
Natural frequency of (30) ω_{β}	-	Slow	-

Table 3
Parameters in numerical simulations.

Parameters	Unit	Value	
Wind turbine	_	NREL 5 MW	
Position of the crane tip p_p	m	$[0, 0, -110]^{T}$	
Hook mass m_h	ton	1	
Yoke mass m_v	ton	20	
Blade mass m_b	ton	17.74	
Blade moment of inertia about COG I_b	kg m ²	4.31e6	
Blade length	m	61.5	
Blade root center position $\{b\}$	m	$[-0.089, -20.51, 0.145]^{T}$	
Position of the sling connection points in $\{b\}$	m	$[0.089, \pm 4.5, 1.855]^{T}$	
Lift wire length	m	9.2	
Lift wire stiffness	N/m	5.59e8	
Sling length	m	9.0	
Sling stiffness	N/m	1e8	
Lift wire and sling damping ratio	_	1%	
Tugger line length l_t	m	20	
Tugger line stiffness	N/m	1e8	
Tugger line damping ratio	-	1%	
Noise power in the position and orientation	W/Hz	1e-8	
Sensor sampling rate	Hz	100	

 Table 4

 Parameters in the controller and reference modules.

Parameters	Value
Matrix K	[5, 500] ^T
Gain matrix C_1	diag{10, 10}
Gain matrix C_2	diag{0.5, 0.5}
Gain matrix C_0	diag{0.05, 0.05}
Natural frequency of the crane reference ω_{β}	0.5
Natural frequency of the blade reference Ω_r	diag{30, 30, 30}

4. Time-domain simulation

4.1. Simulation overview

The simulations are conducted using the MarIn toolbox [19]. In this section, the main environmental and structural parameters are listed in Table 3. In this section, $\Delta z_{b1} = \Delta z_{b2} = 0$. The turbulent wind field is simulated by a mean wind speed $U_w = 10$ m/s and a Mann model (Class C, TI = 0.157). The waves are simulated using a PM spectrum with a significant wave height 1.5 m and wave period 6 s. The simulations last for 1000 s. The sampling frequency for the actuators is 20 Hz. The control gain matrices and necessary parameters in the reference model are tabulated in Table 4. In order to pay more attention to the motion in the x-axis, $k_2 \gg k_1$ in matrix K are selected.

To test the feasibility of the proposed automatic scheme in the three stages, three corresponding simulations are conducted. Three different sets of α_1 , α_2 and ψ_d are used, the tugger line inclinations and desired yaw angle are listed in Table 5. The target of Stage 1 is to stabilize the blade root at the desired position. In the second stage, the crane is involved and the crane boom angle is controlled, meanwhile, the blade follow the crane tip's motion and stabilize the yaw angle. To evaluate the controller performance during the blade transportation, the crane boom rotates from -30 deg to 30 deg and subsequently from 30 deg to -30 deg. In the third simulation (Stage 3), the hub motion is considered to test the hub-motion-tracking capability, and the crane is fixed. The hub motion is calculated by HAWC2 and imported to the simulator offline. Because the influence of the installed blades is very limited, only one monopile motion history is investigated to Stage 3 as an example.

To better analyze the results in each process, a simulation is conducted for each stage, respectively. To avoid

Table 5Tugger line configuration in numerical simulations.

	α_1 (deg)	α_2 (deg)	ψ_d (deg)	β (deg)	Hub motion
Stage 1	-15	15	5	0	No
Stage 2	20	-15	0	±30	No
Stage 3	20	-15	-3	0	Yes

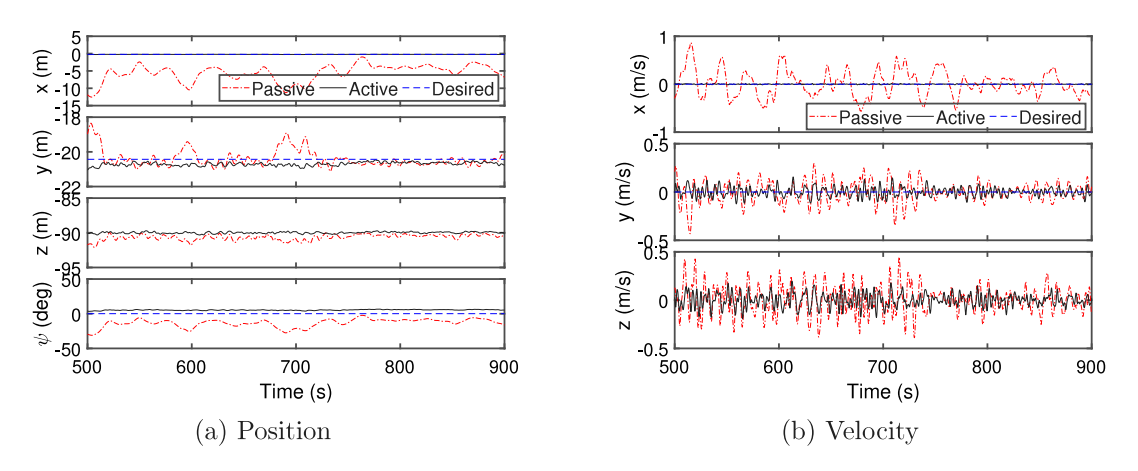


Fig. 10. Root position and velocity history in Stage 1 ($U_w = 10$ m/s, $\alpha_1 = -15$ deg, $\alpha_2 = 15$ deg, and $\psi_d = 5$ deg).

4.2. Simulation results

4.2.1. Stage 1

The simulation results of Stage 1 are presented in Fig. 10. The proposed controller stabilizes both the position and orientation at the suspended blade root well in a turbulent wind field. The blade orientation is maintained at the desired value. Compared to the passive installation approach, the proposed active single blade installation scheme significantly reduces the motion in the x-direction. Though the translational oscillations in the y-axis and yaw angular oscillation still exists, the active scheme effectively prevents the large displacement for the passive scheme at some time instants, e.g., at 600 and 700 s. The amplitude of the angular oscillation is limited into ± 2 deg, which does not restrain the guide pin from plugging into the flange. The velocity at the blade root center is effectively reduced, especially in the global x-axis.

Compared to the results from [20], the root position control is improved, although the tugger line placement is more complex. This is because the controller in [20] is designed according to the blade COG, small oscillation in yaw angle results a large displacement at the root which is 20 meters away from the COG. There exists a constant offset between the real-time and desired position and orientation. This is because of the equilibrium point $(\tilde{p}^*, \tilde{\psi}^*)$ from (13) is not zero. Since the mating operation is not executed, the small offset is not significant. The offset can be compensated by adding the offset into r_d in the reference system. Furthermore, the equilibrium point can be designed by tuning values in K.

4.2.2. Stage 2

The performance of the proposed control scheme in Stage 2 is shown in Fig. 11. There is no desired velocity in the *z*-axis since it is not involved in the controller design. Smaller deviation in the *z*-axis is preferred.

The proposed controller does not deteriorate the motion in the z-axis. The active scheme has a better performance than the passive method. The motion oscillation is largely reduced in the x-axis and yaw angle. During the transportation, the blade root follows the designed trajectory with acceptable accuracy, and the yaw angle derivation is bounded within ± 3 deg. The less critical motions in the y- and z- axes are also regulated to avoid the huge displacement and velocity variance. The displacement in z-axis changes with the crane boom angle. However, the deviation for the active scheme is much smaller than the passive scheme. The dominant motion occurs in the y-axis. The velocities in the x- and y-axes have a sudden drop at 500 s, resulting from the nonsmooth reference trajectory at that time. The drop is quickly stabilized.

We observed that very fast changing crane boom angle β arouses instability and the margin of instability is not explicit. The control law is designed according to several simplified assumptions without high-order system dynamics. For example, $\dot{\alpha}_1$ and $\dot{\alpha}_2$ in $\dot{\theta}_1$ are assumed to be zeros, i.e., the system stability can be influenced with fast changing tugger line inclinations. When the crane boom angle β changes rapidly, the neglected bias in the equilibrium point is no longer small anymore. In addition, the frequency of control input should increase to adjust the increasing system frequency caused by fast crane rotation. A possible way to improve such scenarios is to enlarge the control gain in the controller and enhance the input frequency of the actuator system. However, this may cause system instability and growing budgets for high-performance equipment.

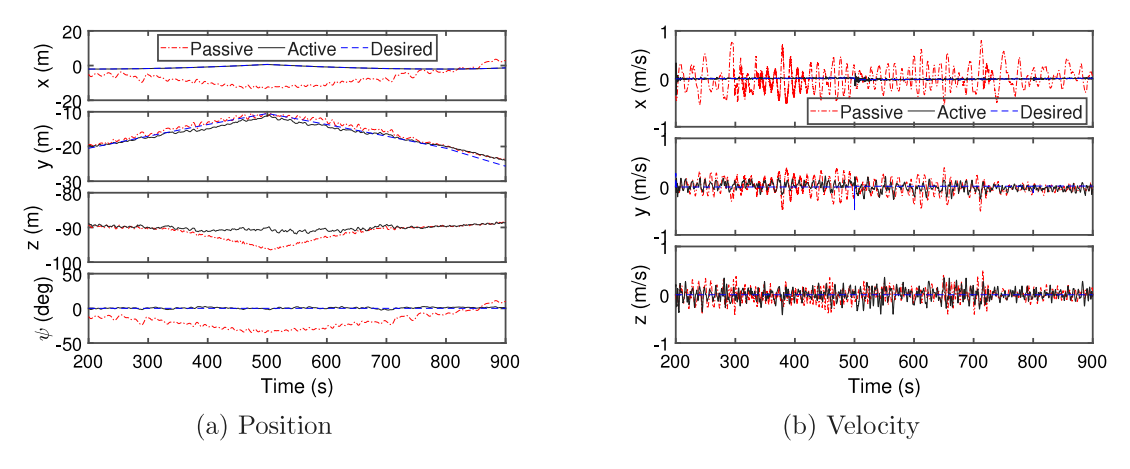


Fig. 11. Root position and velocity history in Stage 2 ($U_w = 10$ m/s, $\alpha_1 = 20$ deg, $\alpha_2 = -15$ deg, and $\psi_d = 0$ deg).

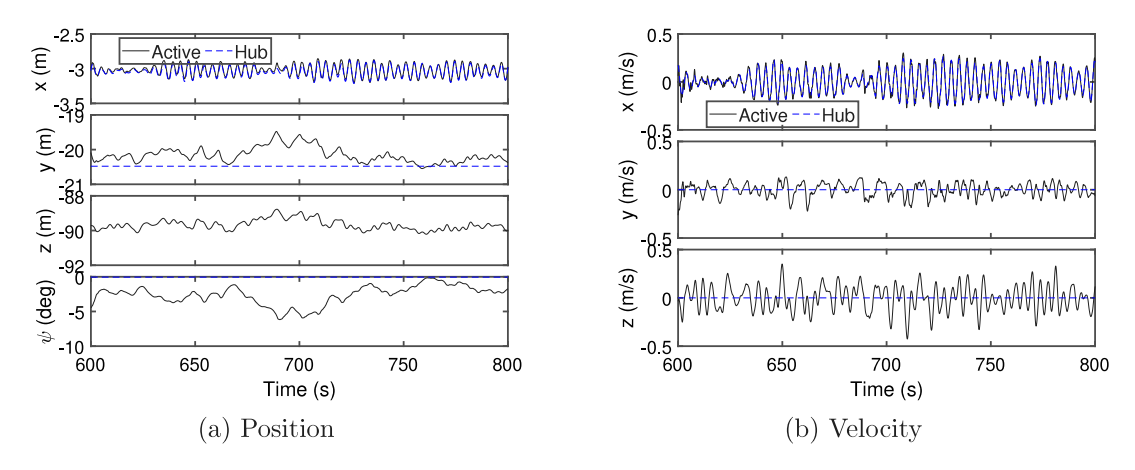


Fig. 12. Root position and velocity history in Stage 3 ($U_w = 10$ m/s, $\alpha_1 = 20$ deg, $\alpha_2 = -15$ deg, and $\psi_d = -3$ deg).

4.2.3. Stage 3

After approaching the mating position, the new objective in Stage 3 is to reduce the relative motion between the blade root and the hub. Simulation results are presented in Fig. 12. Because the passive approach does not have the capability to track the hub motion, its results are not included. With active motion control, it is found that the tugger lines can well compensate the relative motion between the blade root and hub.

5. Sensitivity study and discussion of the proposed autonomous installation scheme

5.1. Simulation overview

In the previous section, the controller is designed based on the assumption that the tugger lines are horizontally arranged, i.e., $\Delta z_{b1} = \Delta z_{b2} \approx z$. The proposed active single blade installation scheme has been validated with time-domain simulation results. However, the tugger line pulleys are not likely to be movable with the suspended blade perfectly in practice. Furthermore, it is difficult to place the tugger line pulleys arbitrary. In this section, sensitivity studies are conducted to evaluate the influence of the tugger line placement to the control system with both horizontal and vertical inclinations in Stage 1 and Stage 3, where the variables are defined in Fig. 2, i.e., (a) α_1 , α_2 , and ψ_d , (b) Δz_{b1} and Δz_{b2} . Accurate motion control in Stage 2 is not necessary; therefore, the corresponding sensitivity study is neglected.

Firstly, a series of simulations are conducted to detect the influence of the tugger line horizontal inclination and the desired yaw angle. A dimensionless factor $\gamma=100(\frac{\psi_d-\alpha_1}{|\alpha_1-\alpha_2|}-0.5)$ is defined to denote the percentage of desired mating orientation ψ_d to α_1 and α_2 , i.e., $\gamma=-50$ denotes $\psi_d=\alpha_1$; $\gamma=50$ denotes $\psi_d=\alpha_2$; and $\gamma=0$ refers to $\psi_d=\frac{1}{2}(\alpha_1+\alpha_2)$. Increasing $|\gamma|$ stands for further away from $\frac{1}{2}(\alpha_1+\alpha_2)$. Normally, tugger line inclinations α_1 and α_2 should be small angles. In the simulations, the variables are selected as $\alpha_i\in\{-20,-15,\dots,15,20\}$ (unit: deg), $\gamma\in\{-100,-90,\dots,90,100\}$, and $\Delta z_{b1}=\Delta z_{b2}=0$. For the sake of simplification, $\beta=0$ in our cases. Note that all the x-, y-, and z-axes in the following discussion are x^c -, y^c -, and z^c -axes, respectively.

In addition, another series of simulations are conducted with $\Delta z_{bi} \in \{-20, -18, \dots, 18, 20\}$ (unit: m) to evaluate the influence of the tugger line vertical inclination. The tugger line inclinations are selected as $\alpha_1 = -15$ deg and $\alpha_2 = 15$ deg. The desired mating yaw angle is $\psi_d = 0$ deg.

The important parameters in Stage 1 are the position and velocity of the blade root center, and the relative displacement and velocity between the blade root center and the hub in Stage 3 are significant. The position and relative displacement are the norm values of 2D motions in x- and z-axes, while the velocity and relative velocity is the norm values in 3D. Normally, the motion maxima keep same trends to the standard derivation (STD) results. The simulations last for 1000 s. To avoid the start-up transient effect, the statistic results are calculated according to the last 500-second history. When the control inputs reach a limitation, the system is considered to be unstable. Moreover, the system may be stable at the beginning and fail to stabilize the system after a few hundred seconds running. Such conditions are considered as unstable simulations.

Simulations using a passive setup are conducted to compare the performance of the proposed active scheme. The tugger lines are shortened by 1.6 m in the first 100 s to provide pretensions. Since the passive cannot change the blade orientation arbitrarily, the comparison is limited to the scenario with $\psi_d=0$ to keep the paper short. Moreover, since the passive scheme fails to meet the tracking requirement in mating operations, the comparison in Stage 3 is not presented.

5.2. Influence of tugger line horizontal inclination

The results of 1512 simulations in Stage 1 and Stage 3 are presented in Fig. 13 and Fig. 14, respectively. Infeasible points are removed either because stabilization of the root motion cannot be achieved or because a negative tension input is required. The black crosses denote the first and last stable points for the specific curve in the simulations. Additional results showing the result of each DOF are presented as appendix in Figs. B.18–B.20.

5.2.1. Stage 1

In Stage 1, we notice that the system stability is influenced by $|\Delta\alpha|$, γ , and $\mathrm{sgn}(\alpha)$ where $|\Delta\alpha| := |\alpha_1 - \alpha_2|$ and sgn is the sign operator. The single blade installation system becomes unstable when $|\Delta\alpha| \le 20$ deg or $|\gamma|$ is larger than some specific values. Normally, the system can be stabilized when the desired yaw angle stays within the range $\gamma \in [-40, 50]$, with $|\Delta\alpha| \ge 25$ deg. The system has different trends at $\alpha_1 \le 0$ and $\alpha_1 > 0$. Since the tugger line 1 is closer to the root and majorly contributes to compensate the wind-induced loads, the influence of the direction of α_1 is more significant than that of α_2 .

For the blade root position STD in Figs. 13(a)–13(b), the performance is better in simulations with $\alpha_1 > 0$. Almost all simulations are stable in the cases $\alpha_1 > 0$. When the sign of α_1 is not changed, the overall performances of different simulations are similar. The blade root oscillation reaches its minimum at the neighborhood of $\gamma = 0$. The STD of root center displacement oscillation grows with $|\gamma|$.

The STD results of the impact velocity are shown in Figs. 13(c)–13(d). Still, $\alpha_1 > 0$ has a preferred performance and broaden parametric selection. When $\alpha_1 \le 0$, blade root velocity STD in all axes increase with $|\gamma|$. When $\alpha_1 > 0$, the trends are different with $\alpha_1 < 0$. The velocity STDs reach their minima when $\gamma = -50$, and enhance w.r.t. the coefficient γ with a very low slope.

From Fig. B.18, when $\alpha_1 \le 0$, increasing $|\gamma|$ reduces the root position standard deviation in the *x*-axis, but enlarges that for the *y*- and *z*-axes. The minimum vertical oscillation is achieved at $\gamma = 50$ when $\alpha_1 > 0$. Larger $|\Delta\alpha|$ improves the velocity STD in the *x*-axis, but negatively influence that in the *y*- and *z*-axes.

5.2.2. Stage 3

In Stage 3, the proposed underactuated control law is more suitable for stabilization problem, instead of tracking control. When $\alpha_1 \le 0$, it is impossible to achieve satisfied performance. The value of k_2 should be small to avoid instability. Otherwise, it may cause a huge yaw angle offset.

The simulation results for the relative position in Fig. 14(a) is very similar to those in Fig. 13(b). The only difference is that the minimum value for Stage 1 is 0.01 m lower than that for Stage 3. Therefore, the proposed controller has a outstanding performance to track the motion in x-direction. The STD for relative velocity in Stage 3 is larger than that in Stage 1; see Fig. 13(d). Since the blade root tracks the hub motion in x-axis well, the performance is not remarkably deteriorated. However, the velocity in y and z direction is introduced by the control law, to some extents. The controller still below the critical impact velocity to ensure the guide pin a good condition. Inspired by such results, the crane should be change to a orientation such that the dominant hub motion stays in the x-direction.

From Fig. B.19, in the dominated hub-oscillation direction, i.e., x-axis, the STD decay with γ . The position error STDs reach their minima near $\gamma = 0$ in the y- and z-axes. The velocity STDs keep a similar trend. The difference is the minima in the y- and z-direction is close to $\gamma = 50$. We notice that the difference is quite limited for $\gamma \in [-50, 50]$. Therefore, $\gamma \in [-50, 50]$ is a good range for the control law.

5.3. Influence of tugger line vertical inclination

The results of 441 simulations in Stage 1 and Stage 3 are illustrated in Fig. 15 and Fig. 16(b), respectively. In the figures, the black crosses stand for the unstable simulations, whose results exceed the specific thresholds indicating stable operations. The red triangles denote the best results, with minimum STD between the mean position and desired position. In Stage 1, the desired position is constant. In a general perspective, the tugger lines can stabilize the blade root motion when the tugger line vertical inclination is limited. Additional results showing the result of each DOF are presented as appendix in Fig. B.21.

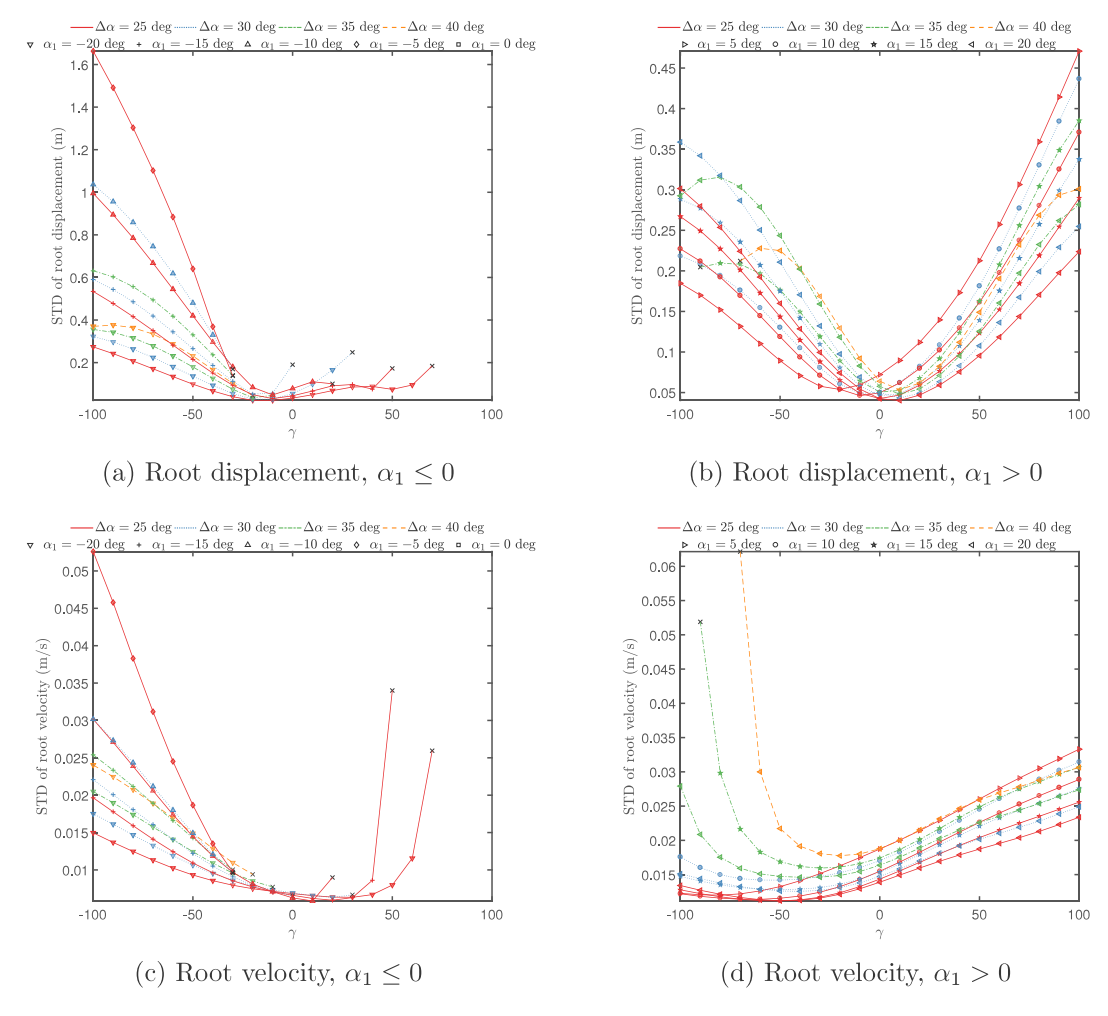


Fig. 13. STD of the blade root displacement and velocity w.r.t. $|\Delta\alpha|$ and γ (Stage 1).

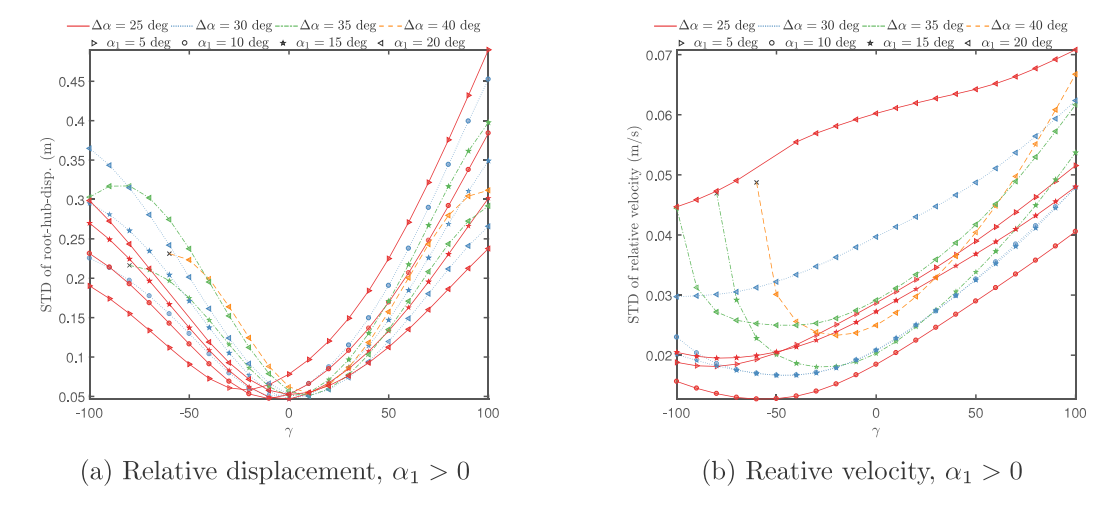


Fig. 14. STD of the relative displacement and velocity between the root center and hub w.r.t. $|\Delta \alpha|$ and γ (Stage 3).

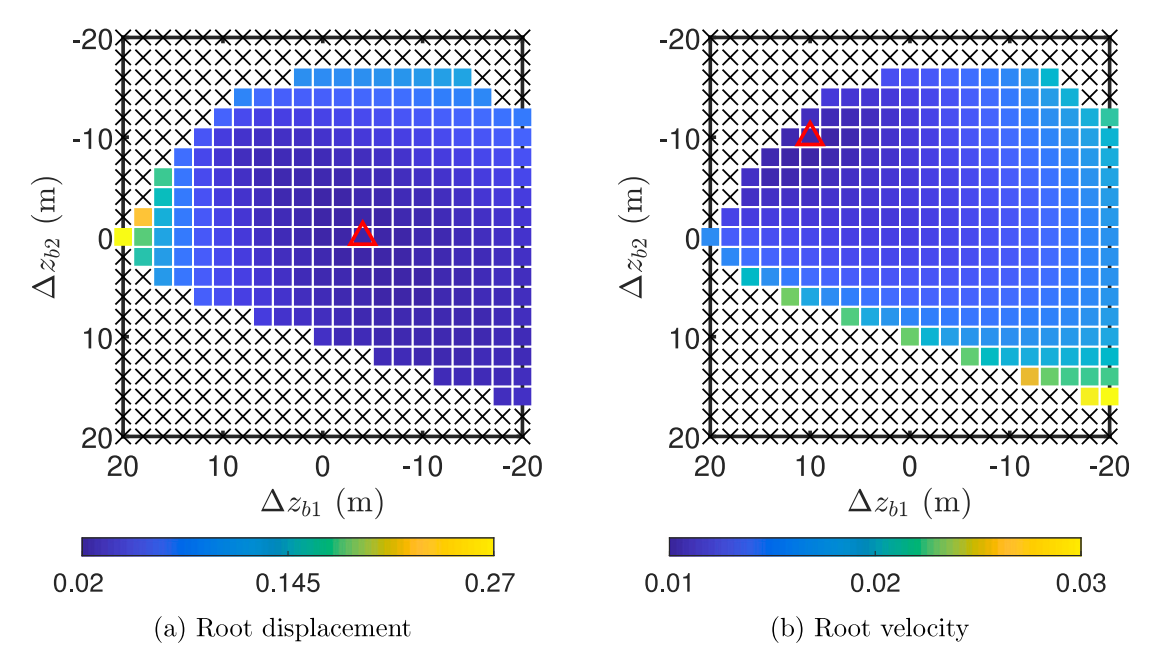


Fig. 15. The influence of the tugger line pulley vertical positions on the STD of the blade root position and velocity (Stage 1).

5.3.1. Stage 1

In Stage 1, the STD of the blade root position in the x-axis is much smaller than those in the other axes. The STD of the blade root position in the y-axes is also well reduced. Though the z-axis is not considered during the controller design process, the blade root motion in the z-axis is satisfied due to the blade's aerodynamic damping. The displacement STD reaches its minimum when Δz_{b1} and Δz_{b2} are closed to zero, i.e., $(\Delta z_{b1}, \Delta z_{b2}) = (-4,0)$. This is because the vertical position of the COG moves up by applying the pretension. Hence, the tugger lines with the pulleys $(\Delta z_{b1}, \Delta z_{b2}) = (0,0)$ are not exactly horizontally arranged after applying the pretension. Additionally, the position of the tugger line 1 pulley is more important since it is the dominated cable. The optimum vertical inclination for the impact velocity is $(\Delta z_{b1}, \Delta z_{b2}) = (10, -10)$. The vertical force components provided by the tugger lines increase with the vertical inclinations. Consequently, very high or low tugger line pulley may cause instability. The difference for the simulations with blue color is very limited. Therefore, when Δz_{b1} and Δz_{b2} are in a safety zone, i.e., $\Delta z_{b1} \in [-10, 10]$ and $\Delta z_{b2} \in [-10, 10]$, satisfied performance can be ensured. When $\Delta z_{b1} = 10$, the vertical inclination angle research 30 deg, which is larger than the critical value for a piratical operation.

5.3.2. Stage 3

Fig. 16 shows that the safety zone in Stage 3 is smaller than that in Stage 1. We notice that the optimal height moves to $(\Delta z_{b1}, \Delta z_{b2}) = (16, 4)$ and $(\Delta z_{b1}, \Delta z_{b2}) = (-2, -2)$ for the relative position and velocity respectively. It is safer to have $\Delta z_{b1} \ge 0$ and $\Delta z_{b2} \in [-10, 10]$. Admittedly, the variance of the tugger line pulley heights influence the performance of the proposed control law. However, the influence is quite small in the safety zone, which is a neighborhood of $(\Delta z_{b1}, \Delta z_{b2}) = (0, 0)$. Therefore, the robustness of the proposed controller is verified.

5.4. Comparison with the passive scheme

The simulation results of the passive scheme in Stage 1 are presented in Fig. 17. Compared with the results using a passive scheme, the proposed active scheme significantly improved the performance of the blade-hub mating operation. The reduction of the displacement and velocity at the blade root is more than 95%. The large STD values are mainly due to the displacement bias caused by the mean wind loads. We note that the control performance depends on the selection of parameters in the controller. In addition, the passive scheme can neither adjust the blade orientation nor achieve hub motion tracking. The blade equilibrium position depends on the wind loads and tugger line configuration, resulting in difficulties to regulate the blade position.

5.5. Discussion and installation highlights

Normally, OWT installation is a short-term operation. The short-term wave-induced motion to a monopile structure at a specific site can be considered as a narrow-band spectrum for both motion amplitude and direction. The proposed controller has a better performance to stabilize the blade root or track the high-frequency motion in the x^c -direction. However, it fails to stabilize the system with rapid changing desired β .

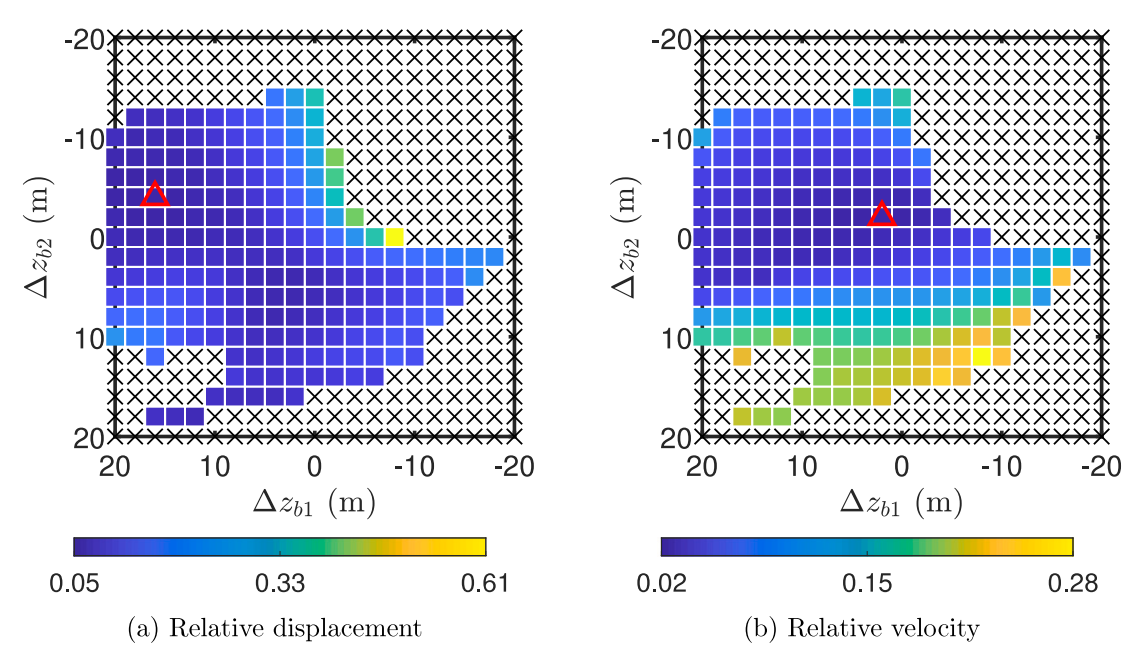


Fig. 16. The influence of the tugger line pulley vertical positions on the STD of the relative position and velocity between the blade root and hub (Stage 3).

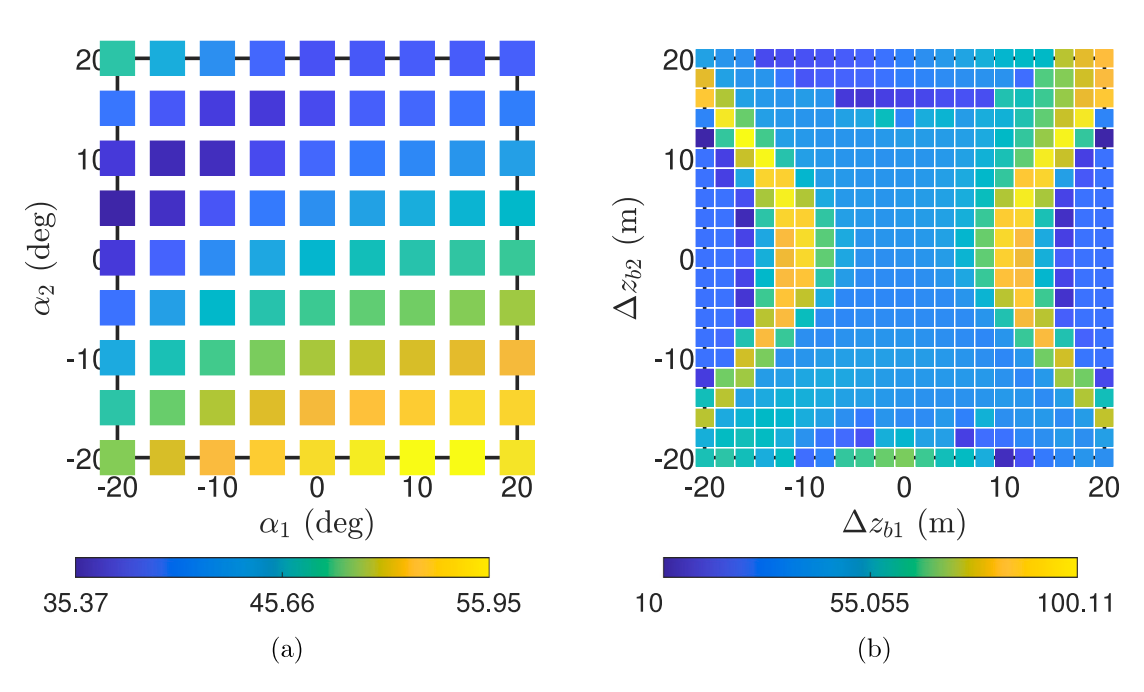


Fig. 17. Displacement STDs at the blade root using a passive scheme (Stage 1, $\psi = 0$) w.r.t. (a) α_1 and α_2 , (b) Δz_{b1} and Δz_{b2} .

The crane is not capable to compensate the spanwise motion. It is challenging to accurately control a large-scale floating crane. Furthermore, the environment-induced monopile hub oscillation is a high-frequency process. As the hub motion mainly stays near the wave incoming direction, a wise choice is to set the boom angle β same to the dominant direction of the hub motion, i.e., the dominant wave heading, which can receive from wave forecast. Since the equilibrium position in y^c -direction depends on the orientation and mean wind speed, the crane tip moves in the opposites direction to compensate such offset.

According to the above sensitivity studies, a few suggestions are given for the tugger-line placement.

- 1. Select a site to jacking up the jackup vessel such that the mating operation can be executed with $\beta = \beta_{wave}$. Then the tugger line is responded to compensate most wave-induced monopile oscillation.
- 2. The horizontal inclination of the tugger line 1 should be greater than 0 deg.

- 3. The difference between the horizontal inclinations should be larger than 25 deg, i.e., $|\alpha_1 \alpha_2| \ge 25$ deg;
- 4. The desired yaw angle should be selected such that the dimensionless coefficient $\gamma \in [-40, 50]$. It is preferred to set the desired yaw angle as the median of α_1 and α_2 , i.e., $\gamma \approx 0$, which can be achieved by controlling the crane;
- 5. The vertical variances of the tugger line pulleys should be within a range of ± 10 meters, i.e., $\Delta z_{bi} \in [-10, 10]$ m; It is preferred to set the pulleys as the same height of the payload.
- 6. Safety factors can be utilized to strictly limit the above data.

The controller performance is accepted for a stabilizing operation, whereas its tracking performance is deteriorated. Since the motion amplitude at the blade root is larger than the hub motion, the control objective in Stage 1 can be adopted in Stage 3 as a weak requirement. Another solution is to introduce other tugger lines to extend the region of the control inputs. After compensating the most critical horizontal motion in the x-axis, efforts should be spent to cancel the vertical oscillation in the z-axis.

6. Conclusion

In this paper, an advanced automatic single blade installation scheme is proposed. In addition to sway and yaw motion, surge motion is also controlled. The system is underactuated with two control inputs and three states. The control law is designed based on backstepping-like technique using a reduced-order error state. The controller can locally asymptotically stabilize the single blade installation system at its equilibrium point.

The influence of installed blades are discussed with numerical simulations in HAWC2. The installed blades slightly decrease the structural natural frequency, and reduce the oscillation amplitude.

The blade mating process is divided into three steps. The simulation results for each step validate that the proposed automatic approach significantly improves the performance compared with typical passive installation method.

Sensitivity studies are conducted to test the effects of the tugger line horizontal and vertical inclinations caused by the pulley placement on the crane. The results show that the proposed scheme has a good performance in a wide scope of tugger line inclination. The tugger line closer to the blade root has a more dominated effect.

Declaration of competing interest

The authors declare that they have no known competing financial interests or personal relationships that could have appeared to influence the work reported in this paper.

Data availability

Data will be made available on request.

Acknowledgments

We appreciate the funding support from the National Key R&D Program of China (2022YFC3801100) and the National Natural Science of China (No. 11872248).

Appendix A. Some variables in the control law

The derivatives of f_1 and f_2 are

$$\begin{split} \dot{f_1} &= \bar{S}\dot{v}r + \bar{S}v\dot{r} + \bar{G}v + \frac{\dot{\tau}_{wn1}}{m} - \bar{G}\dot{p}_p \\ &= \bar{S}(f_1 + G_1u_t)r + \bar{S}v(f_2 + g_2^\top u_t) + \bar{G}v + \frac{\dot{\tau}_{wn1}}{m} - \bar{G}\dot{p}_p \\ &= f_3 + G_3u_t \\ \dot{f_2} &= \frac{\dot{\tau}_{wn2}}{I} - \ddot{\psi}_d \end{split}$$

where $f_3 := \bar{S}f_1r + \bar{S}vf_2 + \bar{G}v + \frac{t_{wn1}}{m} - \bar{G}\dot{p}_p$ and $G_3 := \bar{S}G_1r + \bar{S}vg_2^\mathsf{T}$. Therefore, the time derivative of ϑ is

$$\begin{split} \dot{\vartheta}_1 &= -C_0 z_1 - C_1 (-C_0 z_0 - C_1 z_1 + z_2) + \ddot{p}_d - K[f_2 + g_2^\top u_t - \ddot{\psi}_d + \dot{f}_2 \\ &- \ddot{\psi}_d + \sin\psi \bar{B}_2 \bar{B}_1^{-1} (f_1 - \ddot{p}_d) r - \cos\psi \bar{B}_2 \bar{B}_1^{-1} (f_3 + G_3 u_t - \ddot{p}_d) \\ &+ \cos\psi \bar{B}_2 \bar{B}_1^{-1} (v - \dot{p}_d) r^2 + \sin\psi \bar{B}_2 \bar{B}_1^{-1} (f_1 + G_1 u_t - \ddot{p}_d) r + \sin\psi \bar{B}_2 \bar{B}_1^{-1} (v - \dot{p}_d) (f_2 + g_2^\top u_t)] \\ &= f_4 + G_4 u_t, \end{split}$$

where

$$\begin{split} f_4 := & C_0 C_1 z_0 + (C_1^2 - C_0) z_1 - C_1 z_2 + \ddot{p}_d - K [f_2 - \ddot{\psi}_d + \dot{f}_2 - \ddot{\psi}_d + 2 \sin \psi \bar{B}_2 \bar{B}_1^{-1} (f_1 - \ddot{p}_d) r \\ & - \cos \psi \bar{B}_2 \bar{B}_1^{-1} (f_3 - \ddot{p}_d) + \cos \psi \bar{B}_2 \bar{B}_1^{-1} (v - \dot{p}_d) r^2 + \sin \psi \bar{B}_2 \bar{B}_1^{-1} (v - \dot{p}_d) f_2], \\ G_4 := & - K [g_2^\top - \cos \psi \bar{B}_2 \bar{B}_1^{-1} G_3 + \sin \psi \bar{B}_2 \bar{B}_1^{-1} G_1 + \sin \psi \bar{B}_2 \bar{B}_1^{-1} (v - \dot{p}_d) g_2^\top]. \end{split}$$

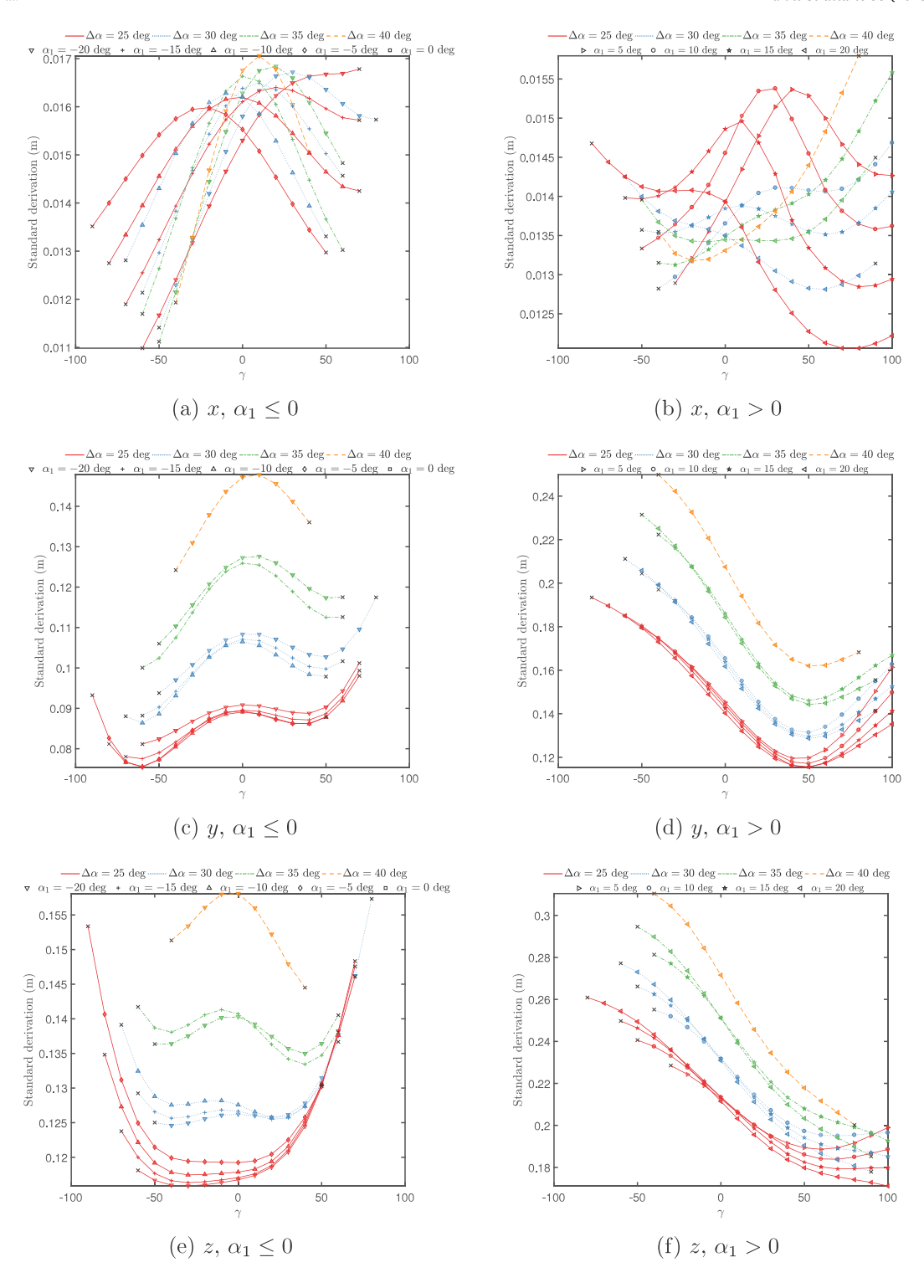


Fig. B.18. Position STD in each DOF w.r.t. $|\Delta\alpha|$ and γ (Stage 1).

Appendix B. Supplementary simulation results

See Figs. B.18-B.21.

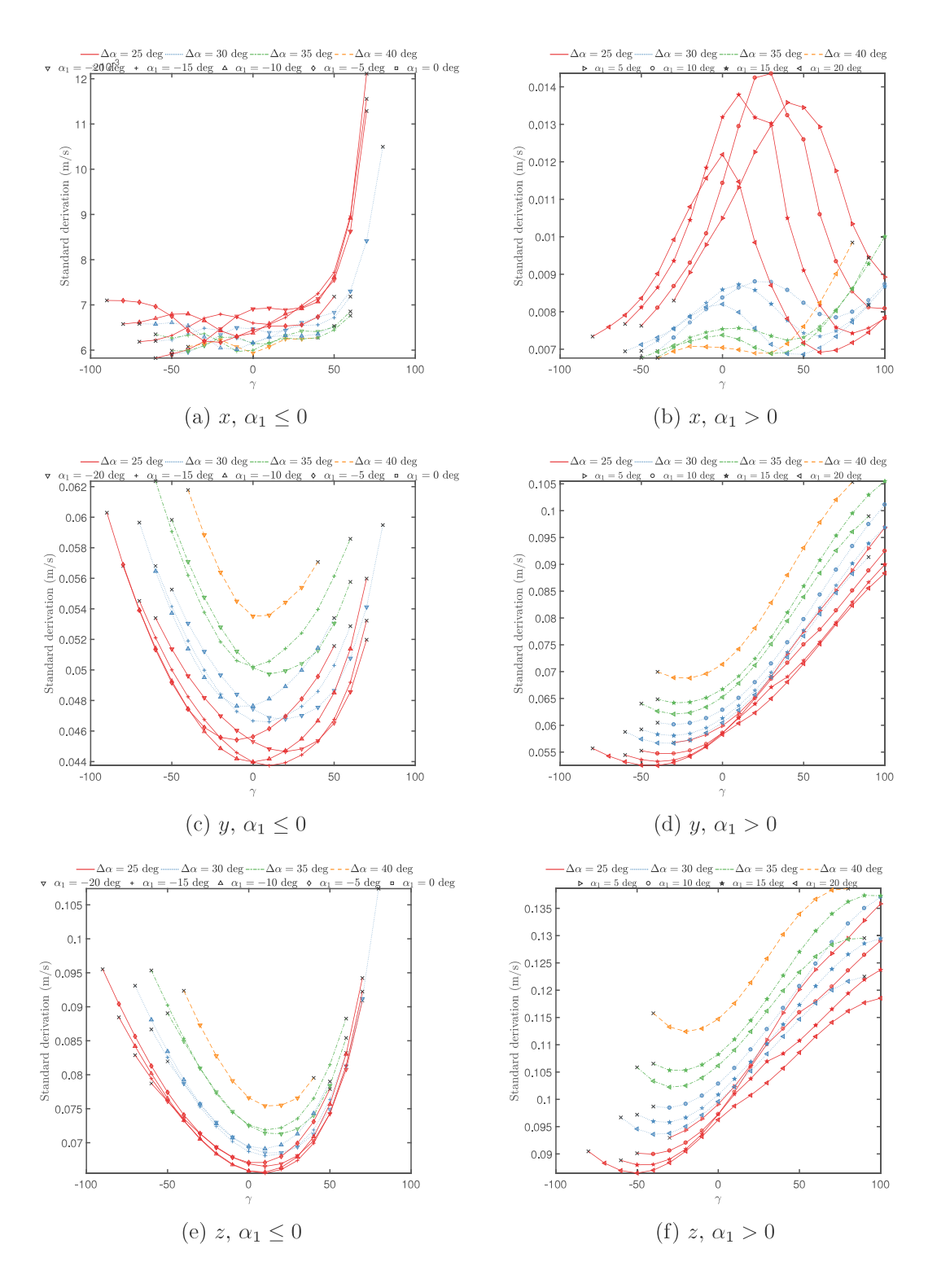


Fig. B.19. Velocity STD in each DOF w.r.t. $|\Delta\alpha|$ and γ (Stage 1).

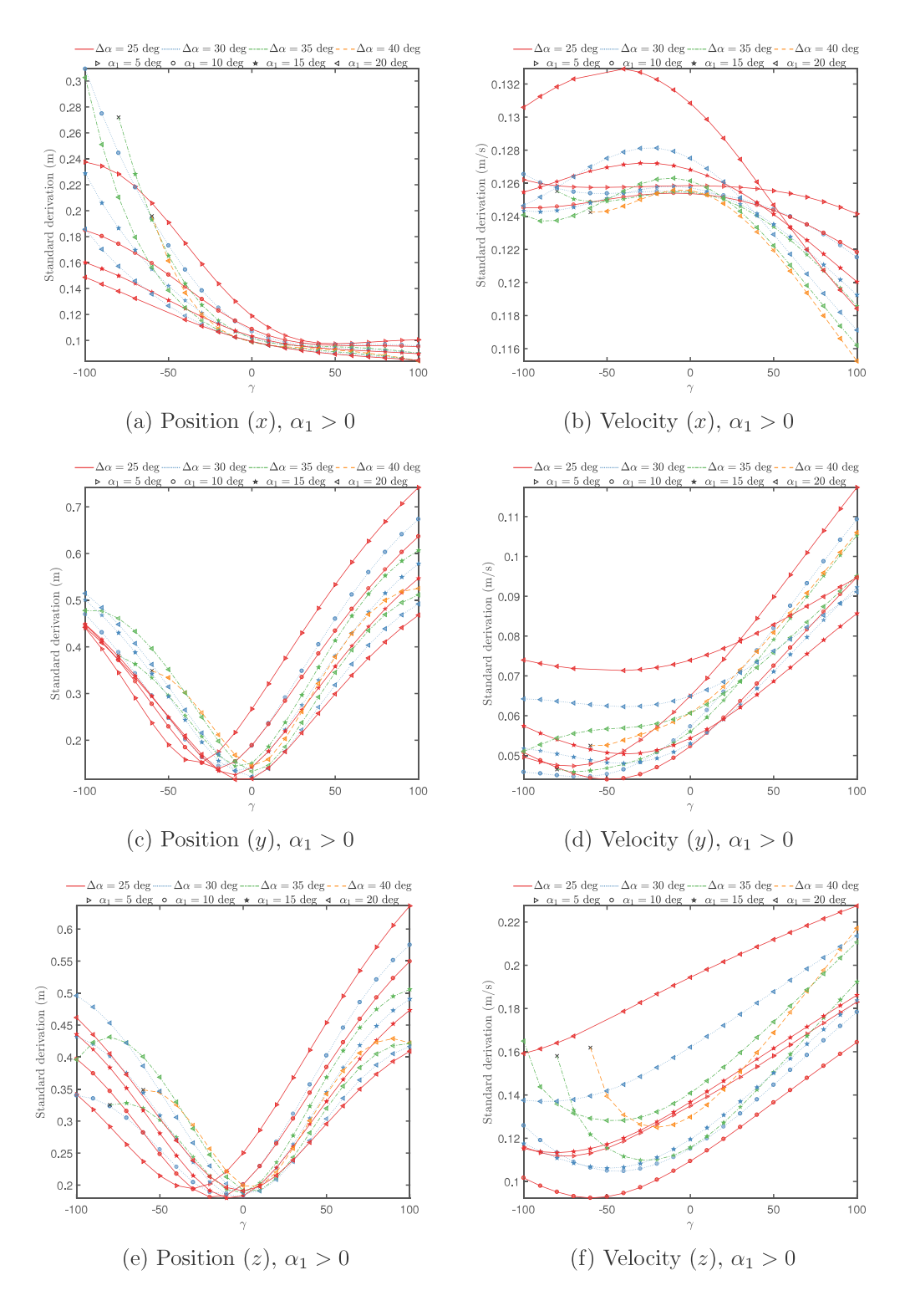


Fig. B.20. Position and velocity STD in each DOF w.r.t. $|\Delta\alpha|$ and γ (Stage 3).

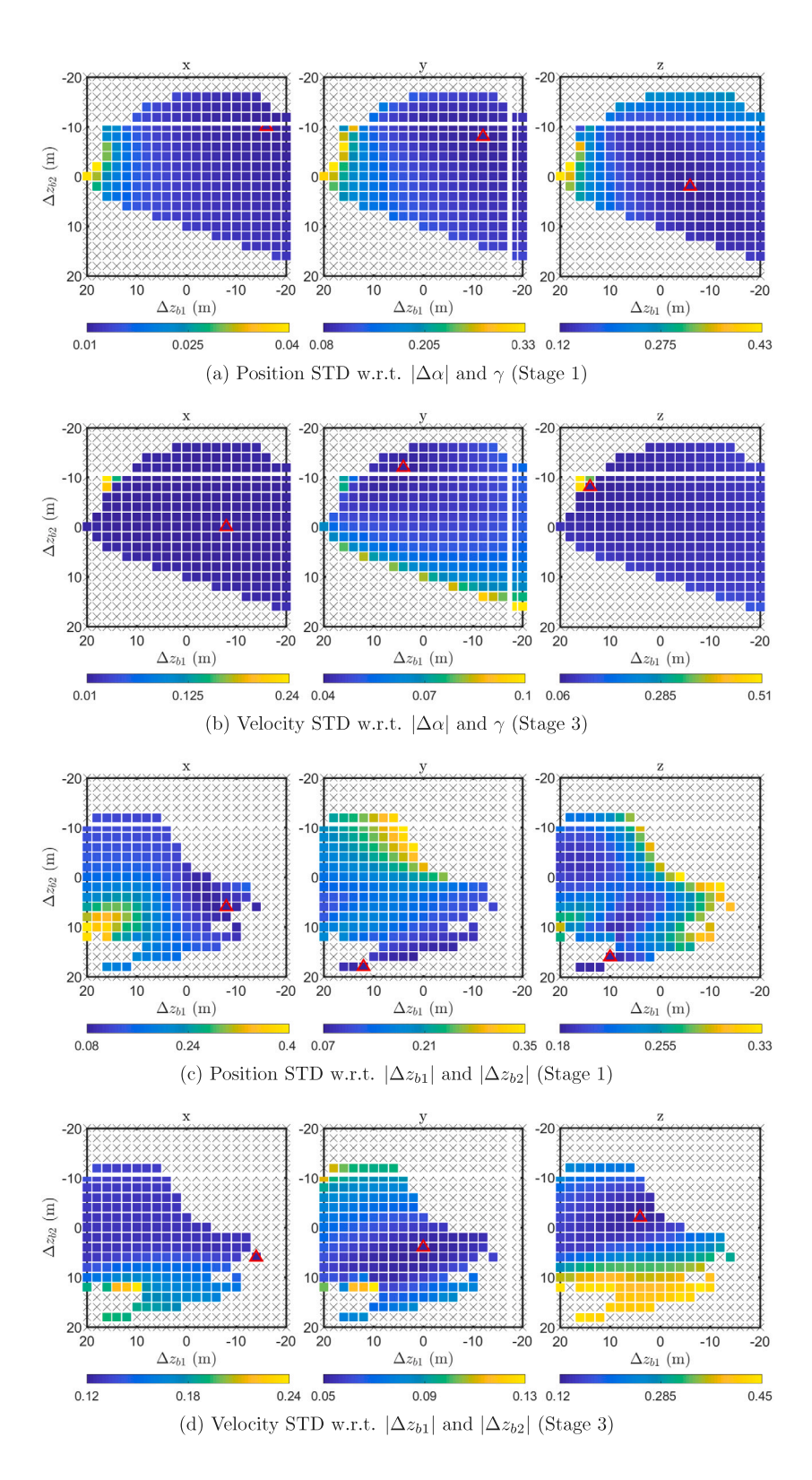


Fig. B.21. The influence of the tugger line pulley positions to the standard derivation of the blade root motion in x-, y-, and z-axes, respectively.

References

[1] Ren Yajun, Venugopal Vengatesan, Shi Wei. Dynamic analysis of a multi-column TLP floating offshore wind turbine with tendon failure scenarios. Ocean Eng 2022;245:110472.

- [2] Gao Zhiteng, Feng Xingya, Zhang Zitan, Liu Zhengliang, Gao Xiaoxia, Zhang Lijun, Li Shan, Li Ye. A brief discussion on offshore wind turbine hydrodynamics problem. Journal of Hydrodynamics 2022;34(1):15–30.
- [3] Barlow Euan, Öztürk Diclehan Tezcaner, Revie Matthew, Boulougouris Evangelos, Day Alexander H, Akartunalı Kerem. Exploring the impact of innovative developments to the installation process for an offshore wind farm. Ocean Engineering 2015;109:623–34.
- [4] Stehly Tyler J, Heimiller Donna M, Scott George N. 2016 Cost of wind energy review. Technical report, Golden, CO (United States): National Renewable Energy Lab.(NREL): 2017.
- [5] Ren Zhengru, Verma Amrit Shankar, Li Ye, Teuwen Julie JE, Jiang Zhiyu. Offshore wind turbine operations and maintenance: A state-of-the-art review. Renew Sustain Energy Rev 2021;144:110886.
- [6] Zhang Lijun, Li Ye, Xu Wenhao, Gao Zhiteng, Fang Long, Li Rongfu, Ding Boyin, Zhao Bin, Leng Jun, He Fenglan. Systematic analysis of performance and cost of two floating offshore wind turbines with significant interactions. Applied Energy 2022;321:119341.
- [7] Martinez A, Iglesias G. Mapping of the levelised cost of energy for floating offshore wind in the european atlantic. Renewable and Sustainable Energy Reviews 2022;154:111889.
- [8] Guo Yaohua, Wang Haijun, Lian Jijian. Review of integrated installation technologies for offshore wind turbines: Current progress and future development trends. Energy Convers Manage 2022;255:115319.
- [9] Breton Simon-Philippe, Moe Geir. Status, plans and technologies for offshore wind turbines in Europe and North America. Renew Energy 2009;34(3):646-54.
- [10] Zhang Puyang, Zhao Xing, Ding Hongyan, Le Conghuan. The wet-towing resistance of the composite bucket foundation for offshore wind turbines. Mar Struct 2021:80:103089.
- [11] Ren Zhengru, Han Xu, Yu Xingji, Skjetne Roger, Leira Bernt Johan, Sævik Svein, et al. Data-driven simultaneous identification of the 6DOF dynamic model and wave load for a ship in waves. Mech Syst Signal Process 2023;184:109422.
- [12] Buljac Andrija, Kozmar Hrvoje, Yang Wenxian, Kareem Ahsan. Concurrent wind, wave and current loads on a monopile-supported offshore wind turbine. Eng Struct 2022;255:113950.
- [13] Wang Yapo, Shi Wei, Michailides Constantine, Wan Ling, Kim Hyungoo, Li Xin. WEC shape effect on the motion response and power performance of a combined wind-wave energy converter. Ocean Eng 2022;250:111038.
- [14] Cheng Min-Yuan, Wu Yung-Fu, Wu Yu-Wei, Ndure Sainabou. Fuzzy Bayesian schedule risk network for offshore wind turbine installation. Ocean Eng 2019;188:106238.
- [15] Chowdhury Nasimul Eshan, Shakib Mahmudul Alam, Xu Fei, Salehin Sayedus, Islam Md Rashidul, Bhuiyan Arafat A. Adverse environmental impacts of wind farm installations and alternative research pathways to their mitigation. Clean Eng Technol 2022;7:100415.
- [16] Aliyar Sithik, Meyer Jannik, Sriram V, Hildebrandt Arndt. Experimental investigation of offshore crane load during installation of a wind turbine jacket substructure in regular waves. Ocean Eng 2021;241:109979.
- [17] Lee Ki-Hak, Jun Sang-Ook, Pak Kyung-Hyun, Lee Dong-Ho, Lee Kyeong-Woo, Park Jong-Po. Numerical optimization of site selection for offshore wind turbine installation using genetic algorithm. Curr Appl Phys 2010;10(2, Supplement):S302–6, The Proceeding of the International Renewable Energy Conference and Exhibition 2008 (RE2008).
- [18] Ziyaei Pegah, Khorasanchi Mahdi, Sayyaadi Hassan, Sadollah Ali. Minimizing the levelized cost of energy in an offshore wind farm with non-homogeneous turbines through layout optimization. Ocean Eng 2022;249:110859.
- [19] Ren Zhengru, Jiang Zhiyu, Skjetne Roger, Gao Zhen. Development and application of a simulator for offshore wind turbine blades installation. Ocean Eng 2018;166:380–95.
- [20] Ren Zhengru, Jiang Zhiyu, Skjetne Roger, Gao Zhen. An active tugger line force control method for single blade installations. Wind Energy 2018;21(12):1344–58.
- [21] Ren Zhengru, Skjetne Roger, Gao Zhen. A crane overload protection controller for blade lifting operation based on model predictive control. Energies 2019;12(1).
- [22] Jiang Zhiyu, Gao Zhen, Ren Zhengru, Li Ye, Duan Lei. A parametric study on the blade mating process for monopile wind turbine installations under rough environmental conditions. Eng Struct 2018;172:1042–56.
- [23] Verma Amrit Shankar, Jiang Zhiyu, Vedvik Nils Petter, Gao Zhen, Ren Zhengru. Impact assessment of a wind turbine blade root during an offshore mating process. Eng Struct 2019;180:205–22.
- [24] Maes K, Roeck G De, Lombaert G. Motion tracking of a wind turbine blade during lifting using RTK-GPS/INS. Eng Struct 2018;172:285–92.
- [25] Ren Zhengru, Jiang Zhiyu, Skjetne Roger, Gao Zhen. Active single blade installation with three tugger lines. In: Proceedings of the 2018 international ocean and polar engineering conference. American Society of Mechanical Engineers; 2018, p. ISOPE2018.
- [26] Khalil Hassan K, Grizzle JW. Nonlinear systems. Vol. 3. Prentice Hall Upper Saddle River, NJ; 2002.
- [27] Power Technology. In pictures the world's longest wind turbine rotor blades. 2013, [Online]URL https://www.power-technology.com/features/featurein-pictures-longest-wind-turbine-rotor-blades. [Accessed 29 Oct 2018].
- [28] Larsen Torben J, Hansen Anders Melchior. How 2 HAWC2, the user's manual. Technical report, RisøNational Laboratory; 2007.
- [29] Mann Jakob. Wind field simulation. Probab Eng Mech 1998;13(4):269-82. http://dx.doi.org/10.1016/S0266-8920(97)00036-2.
- [30] Zhang Yu, Shi Wei, Li Dongsheng, Li Xin, Duan Yuanfeng, Verma Amrit Shankar. A novel framework for modeling floating offshore wind turbines based on the vector form intrinsic finite element (VFIFE) method. Ocean Eng 2022;262:112221.
- [31] Hu Weifei, Choi KK, Zhupanska Olesya, Buchholz James HJ. Integrating variable wind load, aerodynamic, and structural analyses towards accurate fatigue life prediction in composite wind turbine blades. Struct Multidiscip Optim 2016;53(3):375–94.
- [32] Ren Zhengru, Skjetne Roger, Jiang Zhiyu, Gao Zhen, Verma Amrit Shankar. Integrated GNSS/IMU hub motion estimator for offshore wind turbine blade installation. Mech Syst Signal Process 2019;123:222–43.
- [33] Rudra Shubhobrata, Barai Ranjit Kumar, Maitra Madhubanti. Nonlinear state feedback controller design for underactuated mechanical system: A modified block backstepping approach. ISA Trans 2014;53(2):317–26.
- [34] Rudra Shubhobrata, Barai Ranjit Kumar, Maitra Madhubanti. Block backstepping design of nonlinear state feedback control law for underactuated mechanical systems. 2017.
- [35] Kanellakopoulos Ioannis, Kokotović Petar V, Morse A Stephen. Systematic design of adaptive controllers for feedback linearizable systems. In: American control conference, 1991. IEEE; 1991, p. 649–54.